The redox-conditions controlled manganese carbonate mineralization in the Late Paleozoic Qiaerlong deep basin, Western Kunlun Mountains, China

Xi-Yao Li [a,b], Er-Ju Wang [c], Cheng-Quan Wu [a,*], De-Huai Zhao [d,e], Bei Hua [d,e], Zheng-Wei Zhang [a,*], Jin-Hong Xu [a,b], Zi-Ru Jin [a,b]

[a] *State Key Laboratory of Ore Deposit Geochemistry, Institute of Geochemistry, Chinese Academy of Sciences, Guiyang 550081, China*
[b] *University of Chinese Academy of Sciences, Beijing 100049, China*
[c] *Business School of Macau University of Science and Technology, Macau 999078, China*
[d] *Xinjiang Geological Exploration Institute of China Metallurgical Geology Bureau, Urumqi 830063, China*
[e] *Institute of Mineral Resources, China Metallurgical Geology Bureau, Beijing 100131, China*

ABSTRACT

The newly discovered stratiform Mn-carbonate ore from the Zhuwuluke deposit occurs within the fine-grained clastic rocks-carbonate of the Lower Carboniferous Talong Group. Here we utilize petrographical, mineralogical and geological data to shed light on the ore-forming materials sources and metallogenic mechanism of the manganese carbonate mineralization. The ore minerals are composed mainly of Fe-rhodochrosite, rhodochrosite, Ca-rhodochrosite, and kutnahorite. The positive Eu anomalies (average 3.03) of Mn-carbonate ores and Mn-bearing limestones reveal a hydrothermal source. The Mo_{EF} (from 2.09 to 196.18) and U_{EF} (from 0.74 to 3.60) values of most Mn-bearing limestone and wall rock sample suggest that they were deposited under reducing conditions where sulfide was restricted to the pore waters. The higher U_{EF} values of Mn-carbonate ores (mean 24.19) and incomplete separation of Fe from Mn suggest that they were deposited under rapid oxidation conditions. The negative S isotope compositions of pyrite ($\delta^{34}S_{py}$) and Mn-bearing carbonates (average −10.16‰ and −7.17‰, respectively) indicate the microbially mediated diagenetic sulfate reduction (BSR) and a relatively sufficient supply of sulfate in hemipelagic conditions. The C isotope compositions of Mn-bearing carbonates ($\delta^{13}C_{carb}$, average −10.92‰) and its negative correlation with Mn content suggest that the initial Mn precipitated as Mn (oxyhydr)oxides, followed by reduction during burial diagenesis. Apart from that, paragenetic relationships indicate some Mn-carbonates were formed during authigenesis. We suggest that the high contents of Fe in Mn-carbonates were due to rapid oxidation conditions and relatively enough sulfate supply. The redox conditions and relatively stable sedimentary environment during the Early Carboniferous collectively facilitate the formation of manganese carbonate deposit.

1. Introduction

The economical Mn resources in China (mainly sedimentary and supergene Mn ore deposits, Ye et al., 1988) are primarily concentrated in the Mesoproterozoic to Neoproterozoic, the Late Paleozoic, and the Early Mesozoic. These Mn ore deposits are widely distributed in the South China. It has been suggested that the enrichment of Mn and the evolution of the Earth system are closely related, including tectonic movements, volcanic or hydrothermal activity, and climate (Frakes and Bolton, 1984; Liu et al., 2006; Roy, 2006; Maynard, 2010; Haas, 2012). Geochemical data further indicate that the precipitation of Mn in

sediments of different ages was redox controlled (Frakes and Bolton, 1984; Calvert and Pedersen, 1996). Previous researchers mainly focused on manganese ore deposits in South China (Chen et al., 2022; Yan et al., 2022; Gao et al., 2021; Xu et al., 2021), especially well-known Nanhuan (Cryogenian, from 664 to 653 Ma) "Datangpo-type" manganese deposits (Wu et al., 2016), while Carboniferous manganese ore deposits in China are inconspicuous.

The well-known Carboniferous Malkansu Mn-carbonate metallogenic zone in the North Kunlun terrane (Gao et al., 2018; Zhang et al., 2020a,b) formed contemporaneously with the Zhuwuluke manganese carbonate ore deposit (Mao, 2019) hosted in the rocks of the Lower

* Corresponding authors.
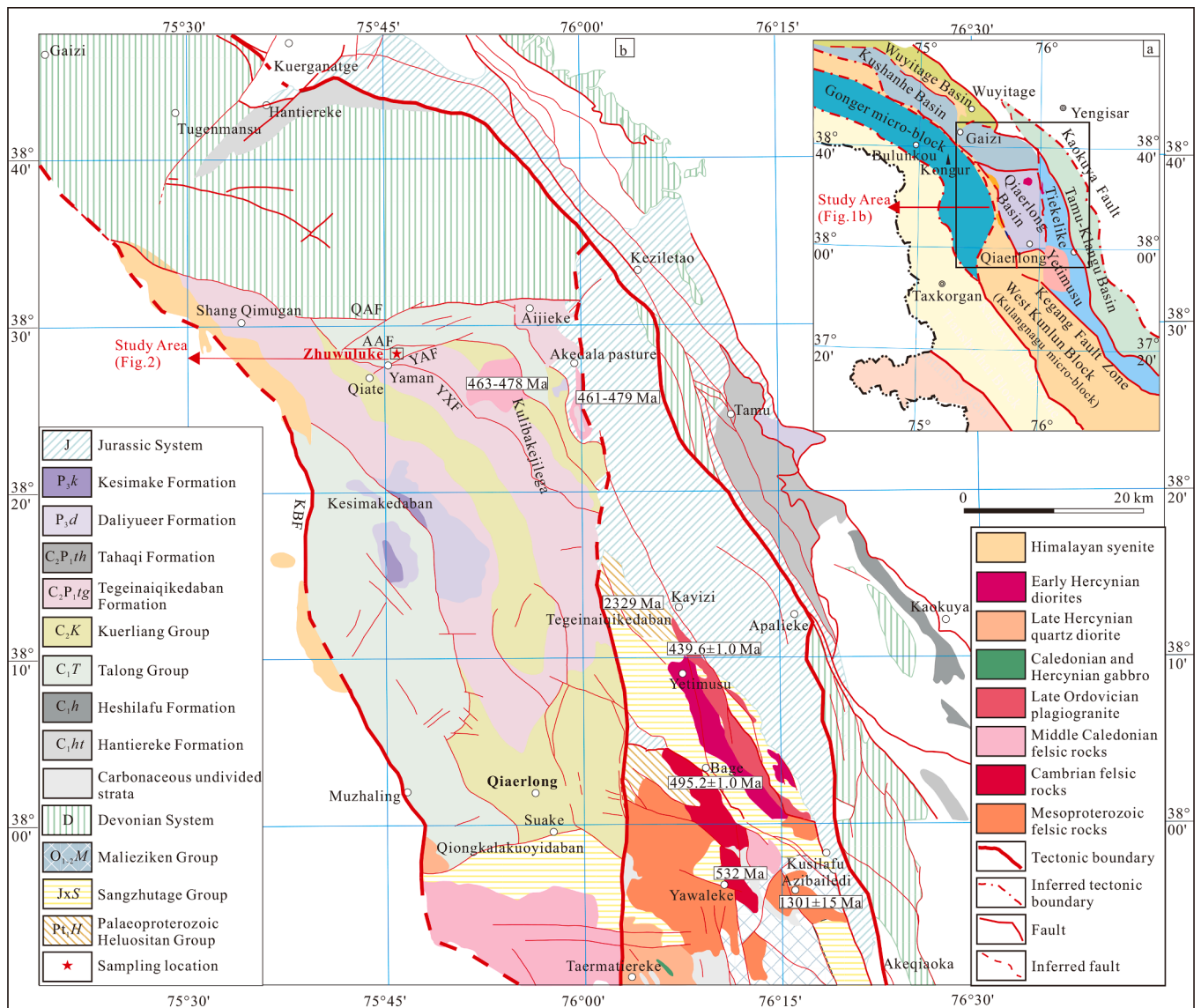 *E-mail addresses:* wuchengquan@mail.gyig.ac.cn (C.-Q. Wu), zhangzhengwei@mail.gyig.ac.cn (Z.-W. Zhang).

Fig. 1. Tectonic sketch (a) and geological map (b) of the Qiaerlong Basin showing major pluton before Carboniferous, modified after Lu and Ren, 2013. KBF = Kongbeili–Muzhaling Fault, QAF = Qimugan-Aijieke Fault, AAF = Aijiekedaban-Aheimaiertai Fault, YXF = Yaman-Xilibili Fault, YAF = Yaman-Aijiekedaban Fault.

Carboniferous Talong Group, a newly discovered Mn-bearing strata in the Qiaerlong Basin. Although previous work mainly focused on the ore-controlling factors and geological features of Mn-carbonate ore bodies in the Zhuwuluke mining area (Mao, 2019), limited information is available on the source of ore materials and mechanism for Mn mineralization and the depositional environment. To aid in resolving both, we present a comprehensive set of field and petrologic data, together with detailed geochemical analyses of Mn-carbonate ores, Mn-bearing limestones, and associated wall rocks of the Zhuwuluke manganese ore deposit, including petrographic observation, bulk geochemistry analysis, electron microprobe analysis (EMPA), and isotope (carbon, sulfur, and oxygen) geochemistry of carbonate and sulfide in this paper. Through this study, we aim to learn the ore-forming materials sources, mineralization process and depositional environment, and to further understand the mechanism of manganese mineralization at Zhuwuluke.

2. Geological setting

The Western Kunlun Mountains region located in the northwest region of the Tibetan Plateau is an important part of the Central Orogenic Belt (Dewey et al., 1988; Jiang et al., 2000). It is a complex accretive orogenic belt with long-term (>500 Ma) evolution, connected to the Pamir tectonic domain and the Altun orogenic belt. It originated from the subduction of the Proto-Tethys Ocean Plate to the northern Tarim Block and the accretion of the Tarim Block southward during the Ordovician to the Triassic (Han, 2006). It is a critical area that provides an ideal opportunity to investigate the Tethys tectonic domain (Fig. 1a, (Pan and Fang, 2010)).

2.1. Features of tectonic blocks and sedimentary formations

The Western Kunlun Block is located between the Kangxiwa and Kegang fault zones. The secondary tectonic units include the Kulangnagu and Gonger microcontinental blocks, the Sangzhutage and Saitula microcontinental blocks. The Kulangnagu microcontinental block bounded by the Kegang ophiolite belt is connected to the southern margin of the Tarim Block. These microcontinental blocks collided in the Early Paleozoic (Pan, 2000; Cui et al., 2006).

The southern margin of the Tarim Block are bounded by the Kaokuya Fault and the Kegang fault zone. The secondary tectonic units include the Tiekelike fault-uplift belt and the Tamu-Kalangu basin. The basement of the Tiekelike fault-uplift belt (Fig. 1a) consists of the
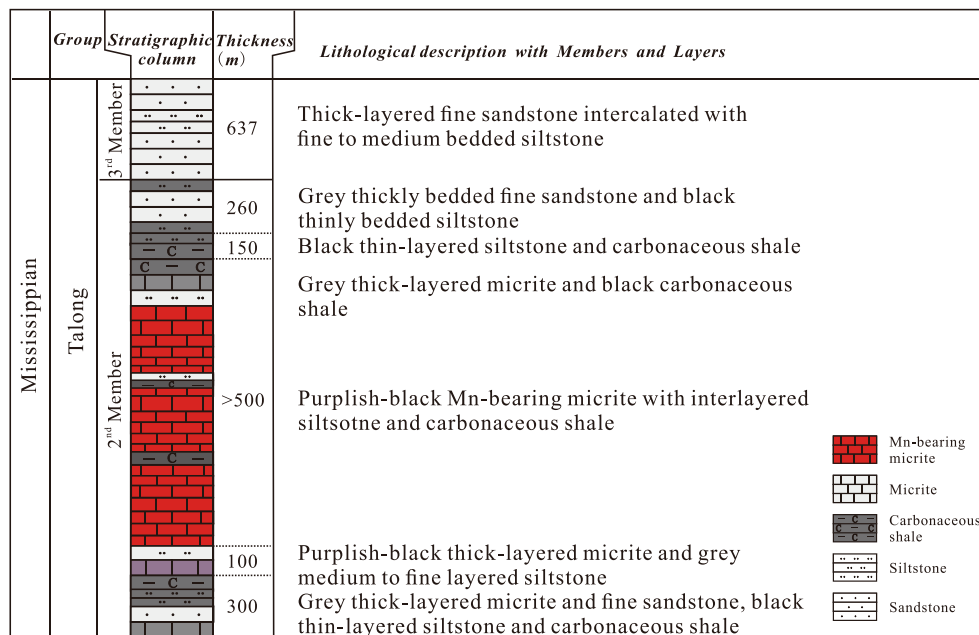
	Group	Stratigraphic column	Thickness (m)	Lithological description with Members and Layers
Mississippian	Talong			

Fig. 2. Stratigraphic chart of the Middle to Upper part of the Talong Group in the Qiaerlong Basin and hosting strata of the Zhuwuluke manganese carbonate deposit.

Table 1
Modal composition of the different members of the Lower Carboniferous Talong Group.

Member	Lithology	Compositions
3rd Member	Clastic rocks	Thickly bedded fine sandstone with interlayered fine to medium-layered siltstone with schistosity
2nd Member (Mn-bearing)	Lutite with interlayered carbonate Manganese carbonate ore	Black argillaceous and carbonaceous shale, grey thickly bedded micrite and beige fine sandstone: quartz, chalcedony, and silicate minerals (feldspar, chlorite, and minor biotite); pyrite Kutnahorite, Mn-siderite, Fe-rhodochrosite, Mn-calcite, siderite, pyrite, Mn- and Fe-oxide

Paleoproterozoic Heluositan Group and Ailiankate Group. The Mesoproterozoic Changcheng Sailajiazitage Group and the Jixian System are cap rock formations. The disappearance of the Lower Paleozoic strata suggests that it was uplifted during the period (Zhang et al., 2021).

2.2. Late Paleozoic back-arc extensional environment and sedimentary basin

The Western Kunlun Block and the southern margin of the Tarim Block collided and formed the Caledonian orogenic belt in the late Early Paleozoic (Cui et al., 2006; Xu et al., 2011). However, the Western Kunlun Mountains area was still in a multi-island ocean environment in the early Late Paleozoic, and a suite of sedimentary sequences representing transgression developed simultaneously, indicating an extensional environment (Zhang et al., 2021).

The subduction of the Kangxiwa oceanic crust toward the Western Kunlun Block resulted in the formation of the Aoyitage-Kuerliang back-arc basin belt (Cui et al., 2006). The Qiaerlong Basin is one of them and it is located along the northern margin of the Western Kunlun block.

2.3. Basin sedimentary construction and magmatic activity

The Qiaerlong Basin, is located south of the Kushanhe basin and bounded by the Qimugan-Aijieke Fault. The Carboniferous to the Permian strata are widely distributed in the Qiaerlong Basin with developed NW-trending folds and faults (Fig. 2, Table 1). Rocks of the Lower Carboniferous Talong Group with microfossils (sporopollen) and tetracoral fossils (Cai, 1992) comprises bathyal clastic rock intercalated with clastic rock (Xie et al., 2018). It has fault contact with the overlying rocks of Upper Carboniferous Kuerliang Group. The rocks of the Kuerliang Group is characterized by turbidite, gravel-bearing quartz siltstone, mudstone, and sandstone of the platform (Lu and Ren, 2013). The Akedala pluton in the northern Qiaerlong Basin is the only Late Paleozoic arc magmatic rock discovered to date (Xu et al., 2019, 2021).

3. Geological characteristics of the Zhuwuluke manganese ore deposit

The Zhuwuluke manganese carbonate ore deposit is in the Qiaerlong–Aijiekedaban mineralization subzone and it is near the northern margin of the Qiaerlong Basin. It is surrounded by the Aijiekedaban-Aheimaiertai Fault, Yaman-Xilibili Fault, and Yaman-Aijiekedaban Fault (Figure 1b).

3.1. Strata and structures

The strata exposed in the mining area are sedimentary rocks of the Talong Group, including sandstone, siltstone, and limestone (Fig. 3). The Mn mineralization is hosted in the siltstone and limestone. It is NW striking with steep dips to the NE at 55 to 73°. The surface of the outcrop shows yellowish-brown color due to supergene weathering. It can be subdivided into four layers: (1) The first mainly comprises gray thick-layered limestone, gray to gray–brown medium- to thick-layered fine sandstone, black thinly layered siltstone, and carbonaceous shale. (2) The second is the host rock of the manganese carbonate ores, showing obvious sedimentary rhythm of interlayered carbonaceous shale and siltstone (Fig. 4a, b). (3) The third is composed mainly of black thin-layered siltstone and carbonaceous shale. (4) The fourth consists of gray to gray–brown thick-layered siltstone and thinly bedded siltstone (Mao, 2019).

Exposed strata in the mining area are involved in the Late Paleozoic Qiaerlong anticlinoria. Developed folds and faults can be divided into three groups: nearly EW-, NW-, and NE-trending (Mao, 2019). Frequent small-scaled structural activities (Fig. 4a) deformed the Mn orebody
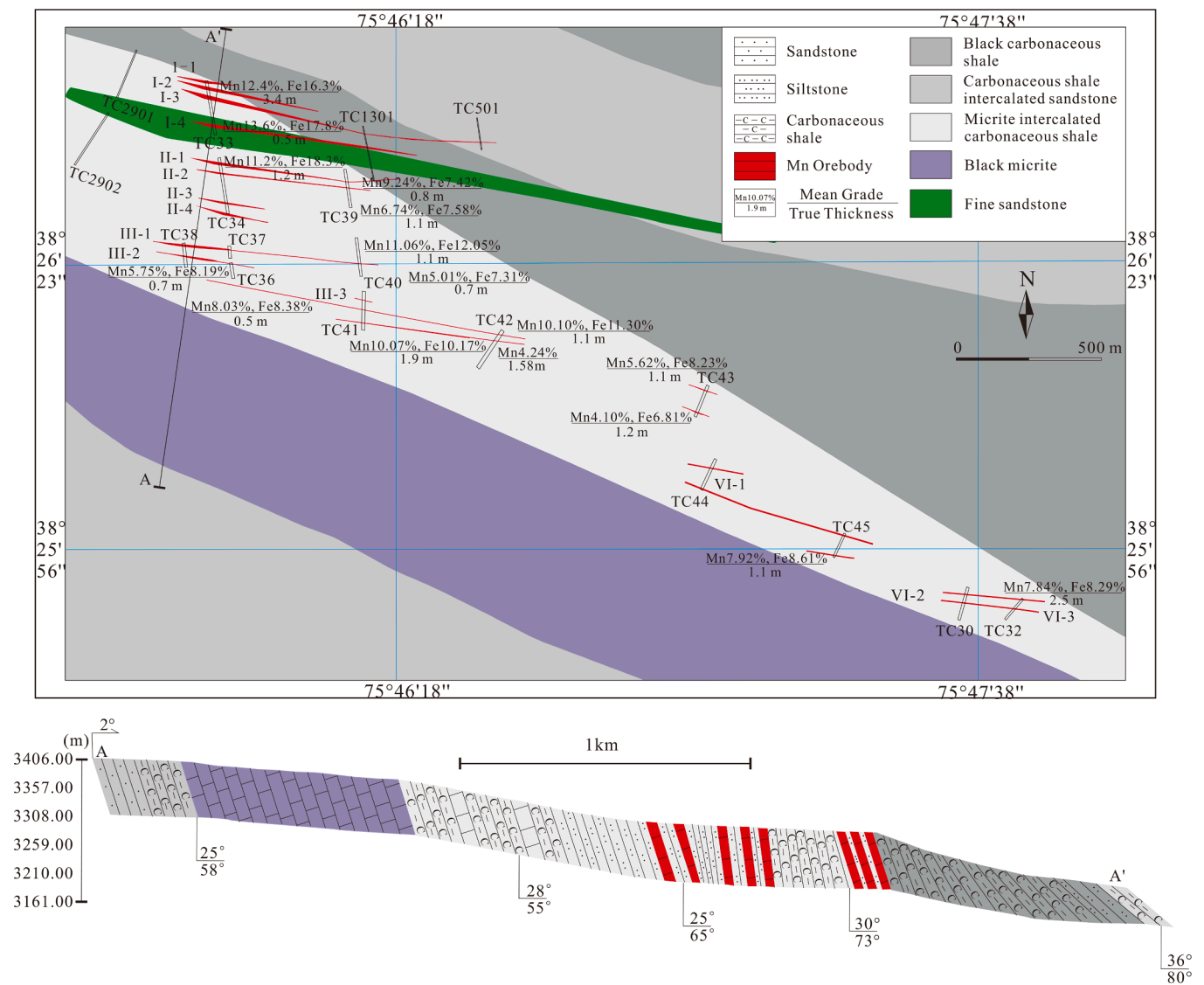
Fig. 3. Geological map of the Zhuwuluke manganese carbonate ore deposit in the Qiaerlong Basin, Western Kunlun Mountains (modified after the prospecting report of the Xinjiang geological exploration institute of China metallurgical geology bureau), and profile A-A' shows the south wing of the syncline of mining area.

locally.

3.2. Characteristics of manganese ore bodies

Generally, seventeen Mn-bearing layers, approximately 1 to 5 m in thickness, occur in the mining area (Fig. 3). Ore bodies generally occur as stratiform and lentoid. The hanging wall and foot wall of the manganese ore bodies are both micrite (Mao, 2019). The characteristics of the primary orebodies are summarized in Table 2.

The manganese carbonate ores mainly show massive and nodular structures (Fig. 4c-d). Manganese carbonates are the most common manganese-rich minerals, and they dominate the mineralogical composition of the ore zone. The manganese carbonate is invariably a mixed Mn-Fe-Ca-Mg phase rather than pure rhodochrosite (Fig. 4e-g). Some occurrences have compositions that are close to ideal kutnohorite [$Mn,Ca(CO_3)_2$,((Calvert and Price, 1977)], including kutnahorite [$Ca_{1.02}(Mn_{0.44}Mg_{0.31}Fe_{0.24})(CO_3)_2$] and Fe-rhodochrosite [$(Fe_{0.44}Mn_{0.37}Mg_{0.11}Ca_{0.08})CO_3$], Mn-siderite [$(Mn_{0.41}Fe_{0.37}Ca_{0.14}Mg_{0.08})CO_3$], and Ca-rhodochrosite [$(Mn_{0.56}Ca_{0.11}Fe_{0.10}Mg_{0.06})CO_3$] (Table 3). The granular Ca-rhodochrosite (Fig. 4e-f) and amorphous Fe-rhodochrosite are most common ore minerals (Fig. 4g). In the manganese carbonate sample ZWLK-22, some carbonate grain show a Mn-rich rim (Fig. 4f).

Beyond that, some hydrothermal rhodochrosite vein fill the Fe-calcite cracks (Fig. 4e-g).

The gangue minerals mainly comprise dolomite and calcite (Fig. 4e-g). Disseminated euhedral–subhedral granular pyrite is common in some samples (Fig. 4d), especially wall rock samples, with sizes from 0.4 to 2 mm.

In general, there are three main stages during the manganese carbonate mineralization process at Zhuwuluke: sedimentary-diagenetic period, hydrothermal period and supergenetic oxidation period (Fig. 5). The sedimentary-diagenetic period is of most importance to the mineralization.

4. Sampling and analytical method

A total of 31 samples, including five Mn-carbonate ores, 20 Mn-bearing limestones, and six wall rock samples, were obtained from exposed strata and underground mine tunnels at the Zhuwuluke mine. Several modern analytical methods were used in the research, including elemental and isotopic geochemistry studies, to learn the mineralization mechanism and depositional environment of the Mn-carbonate deposit.

Representative samples were chosen for observation under a microscope and EMPA to determine mineralogy and paragenesis. Based on
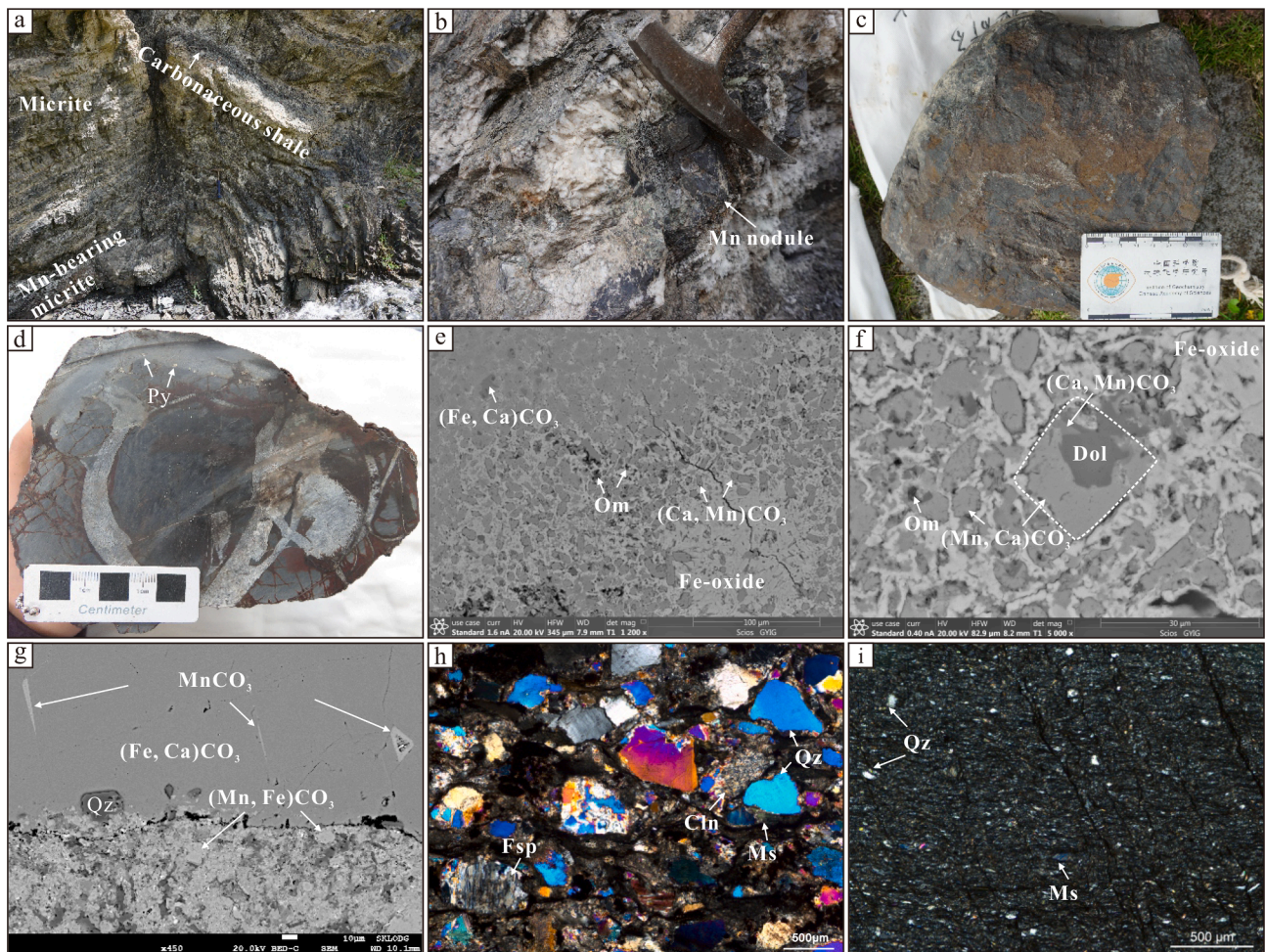
Fig. 4. Field photos and photomicrographs showing typical structures of manganese carbonate ores, representative textures and petrographic features of the 2nd Member of the Talong Group at the Zhuwuluke mine. a. Mn-bearing micrite interbedded with carbonaceous shale and sandstone; b. Mn nodule; c. Massive manganese carbonate ore; d. Manganese carbonate nodule with euhedral pyrite; e. Granular Ca rhodochrosite in the manganese carbonate ore (sample ZWLK-22, BSE image); f. Dolomite with Mn-calcite rim (BSE image); g. Amorphous Fe-rhodochrosite and rhodochrosite veins (BSE image); h. Interlayered sandstone (plane-polarized light); i. Wavy laminations, quartz and muscovite detrital in carbonaceous shale (plane-polarized light). For abbreviation: BSE = backscattered electron image; Cln = chalcedony, Qz = quartz, Py = pyrite, Dol = dolomite, Om = organic matter, Ms = muscovite, Fsp = feldspar.

detailed petrology identification, samples without alteration and veins were crushed to a 200-mesh size for geochemical analyses. Most of the experiments were performed at the State Key Laboratory of Ore Deposit Geochemistry, Institute of Geochemistry, Chinese Academy of Sciences (CAS), and organic carbon analyses were undertaken at the Key Laboratory of Environmental Geochemistry, Chinese Academy of Sciences. The backscattered electron images were taken by FIB/SEM dual beam system in Center for Lunar and Planetary Sciences, and FE-SEM in the State Key Laboratory of Ore Deposit Geochemistry, Institute of Geochemistry, CAS.

Major elements were determined at Thermo Fisher ARL Perform X 4200, using an X-ray fluorescence (XRF) spectrometer, and the method was documented by (Hu, 2009). The detection limit for all major oxides is 0.01 wt%, and the analysis errors were less than 10 wt%. The analysis errors were less than 3 wt%. Trace element (including rare earth elements, hereafter REEs) concentrations were analyzed using an inductively coupled spectrometry (ICP-MS) analytikjena PlasmaQuant MS Elite, and the method was documented by Qi et al. (2000).

EMPA was conducted using a JXA-8230 Hyper Probe with a 10 μm beam diameter, 25 kV accelerating potential, and 10 nA probe current. Natural mineral Mn standards were used for the Mn-rich minerals. The data were reduced using the ZAF correction method.

All samples from the Zhuwuluke Mn ore deposit were selected for

organic carbon content and $\delta^{13}C_{org}$ analyses. In addition, $\delta^{13}C_{carb}$ was determined from two Mn-carbonate ores and seven Mn-bearing carbonate samples. Samples consisted of 3.0 g portions that were sieved through a 200-mesh size screen; after weighing, the samples were placed into 50 ml centrifuge tubes. To remove inorganic carbonate, the samples were reacted with 6 mol/L hydrochloric acid and oscillated every at least two hours. Then, the residues were washed with deionized water until they reached neutral conditions. The residues were dried at 60 °C, and the organic carbon contents were analyzed using an organic elemental analysis apparatus (the instrument was a vario MACRO cube). The organic carbon isotopes were analyzed with a MAT251EM mass spectrometer. The inorganic carbon isotopes were analyzed with a MAT253 mass spectrometer. The carbon isotope data are expressed by using international standard V-PDB (Vienna Pee Dee Belemnite) values as follows: $\delta^{13}C_{V-PDB}$ (‰) = $[(^{13}C/^{12}C)_{sample}/(^{13}C/^{12}C)_{standard} - 1] \times 1000$, $\delta^{18}O_{V-PDB}$ (‰) = $[(^{18}O/^{16}O)_{sample}/(^{18}O/^{16}O)_{standard} - 1] \times 1000$.

Eight Mn-bearing limestone samples in addition to one Mn ore sample, of which bulk sulfur concentrations >2 wt%, were chosen to detect the bulk $\delta^{34}S$ compositions. The samples were pretreated by sodium carbonate-zinc oxide fritting to transform S^{2-} into SO_4^{2-} and finally obtained $BaSO_4$ by adding excess $BaCl_2$ solution. The detailed process is as described as follow. Firstly, the 200-mesh sample powder containing around 15 mg of sulfur was placed in an 18-ml ceramic crucible, mixed

Table 2
Overview of Mn ore bodies and sample location.

No.	Orebody No.	Length (m)	Thick (m)	Trend	Dip	Mn + Fe Grade	Sample	Mineral Compositions
1	I-1	90	4.44	100°	10°	18%	ZWLK-28	Siderite, Pyrite, Fe-oxide
2	I-2	190	0.59–6.80	100°	15°	18%	ZWLK-24	Rhodochrosite, Calcite
3	I-3	1000	0.95–10.13	105°	65°	22–33%	ZWLK-22	Rhodochrosite, Dolomite, Mg-calcite
4	I-4	650	4.73	100°	70°	23%	ZWLK-20	Ca-rhodochrosite, Mn-oxide
5	II-1	490	5.02	100°	65°	18%	ZWLK-18	Fe-rhodochrosite, Rhodochrosite
6	II-2	480	0.79–2.26	130°	65–70°	16%	ZWLK-15	Ca-rhodochrosite, Apatite
7	II-3	100	1.07–2.64	130°	75°	17%	ZWLK-13	Rhodochrosite, Py, Calcite
8	II-4	130	4.64	115°	65°	20%	ZWLK-12	Rhodochrosite, Sid, Py
9	III-1	740	0.51–3.48	95°	55°	16–22%	ZWLK-8	Rhodochrosite, Mn-calcite, Mn-oxide, Mn-siderite, Apatite
10	III-2	240	0.56–0.61	100°	70°	21%	ZWLK-7	Fe-oxide
11	III-3	1020	0.65–1.37	100°	55–70°	10–15%	ZWLK-5	Fe-rhodochrosite, Rhodochrosite, Mn-calcite, Calcite, Dolomite, Apatite
12	III-4	600	1.58–1.90	100°	55–70°	21%	ZWLK-2	Todorokite, Fe (Mn)-calcite, Fe-oxide
13	IV-1	680	1.55–2.24	110°	55–70°	12–17%		
14	IV-2	350	2.22	95°	55–70°	15%		
15	IV-3	340	2.63–3.17	95°	55–70°	15%		
16	V-1	440	0.5	88°	52–60°	28%		
17	V-2	420	0.5	88°	5°	30%		

with 8 g of Ischka reagent, and then placed on a layer of Ischka reagent Secondly, the crucibles were placed into the muffle and kept heated at 800 °C for 1 h. After cooling, the samples were put into hot water for extraction, and several drops of ethyl alcohol were added to reduce the green potassium manganate. Thirdly, the samples were boiled for several minutes, crushed and filtered with qualitative filter paper. Several drops of methyl orange were added to the filter liquor, the beakers were washed with 6 mol/L sodium carbonate 4–5 times and precipitated 7–8 times. Then, several drops of methyl orange were added to the solution, and 6 mol/L hydrochloric acid was used to neutralize the solution until excess for 3 ml. Fourthly, the solution was diluted with deionized water to 300 ml and then it was boiled to remove carbon dioxide, and 10–15 ml 0.5 mol/L barium chloride solution (depending on the sulfur content). Fifthly, the solution was boiled again for 0.5 h and kept for >4 h. Then, the precipitation was filtered through quantitative paper, and hot deionized water was added until no Cl occurred (tested by silver nitrate solution). Finally, the filter paper was carbonized and precipitated in a 10-ml ceramic crucible (firing at 800 °C for 1 h). After cooling, $BaSO_4$ was extracted successfully.

A continuous flow isotope ratio mass spectrometer (CF-IRMS) (EA-IsoPrime instruments) was used to analyze the $\delta^{34}S$ of the Mn-bearing carbonates. The measured data are expressed by using international standard sulfur isotope CDT (Canyon Diablo Troilite) values and sulfur isotope standards GBW 04,414 (Ag_2S, $\delta^{34}S_{CDT} = -0.07 \pm 0.13‰$) and GBW 04,415 ($Ag_2S$, $\delta^{34}S_{CDT} = 22.15 \pm 0.14‰$) as follows: $\delta^{34}S$ (‰) = $[(^{34}S/^{32}S)$ sample$/(^{34}S/^{32}S)$ standard $- 1] \times 1000$. The analytical uncertainties for $\delta^{34}S$ are better than 0.1‰ (2σ).

Pyrites from three Mn-bearing carbonate samples were chosen for in-situ sulfur isotope analysis. The measurements were performed on a Nu Plasma III MC-ICP-MS (Nu Instruments) attached to a RESOlution-155 ArF193-nm laser ablation System (Australian Scientific Instruments). The mass separation was calculated as 0.3333 in the analyses. The instrument was operated in pseudo-medium resolution mode (Millet et al., 2012) to resolve polyatomic interferences from $^{16}O-^{16}O$ for ^{32}S and $^{16}O-^{18}O$ for ^{34}S, adjusting the source slit to medium (0.05 mm) in conjunction with using the alpha slit. Sulfide was ablated in a mixture of helium (350 ml/min) and nitrogen (2 ml/min) atmosphere using the following parameters: 20 s baseline time, 40 s ablation time, 40 s wash time, 60 μm spot size, 6 Hz repetition rate and 2–3 J/cm^2 energy density. All analyses followed standard sample bracketing procedures of three

samples bracketed by pyrite pressed powder Tablet (PSPT-2) (Bao et al., 2017; Chen et al., 2019). Two in-house standards consisting of natural pyrite crystals (SB-1 from the Shangbao W-Sn deposit and HYC-1 from the Huayangchuan Nb-U-REE deposit, China) every five unknown samples were treated as quality controls. The measured $\delta^{34}S_{V-CDT}$ values for the standard were 16.57‰ (n = 12) for SB-1 and −5.76‰ for HYC-1 (n = 12), which were identical to the recommended values (16.57‰ for SB-1 and −5.76‰ for HYC-1) (IRMS).

5. Results

5.1. Major elements

The major elemental compositions of the rocks of the Middle Member in the Talong Group are marked by considerable variations (Table 4, Fig. 6). Five samples of Mn ore from the Talong Group are characterized by higher Mn (10.09 to 16.59 wt%), Fe contents (8.86 to 19.36 wt%), and P contents (1.12 to 2.60 wt%). The Mn enrichment factor (Mn_{EF}) was highly elevated, with values ranging from 1849 to 4175 with a mean of 2979. Conversely, the values of Fe_{EF} are relatively small, with a range of 37 to 80 and a mean of 54. Mean concentrations of other significant oxide concentrations within the Mn-carbonate ores are low, including SiO_2 (17.58 wt%), Al_2O_3 (1.92 wt%), CaO (14.33 wt%), and MgO (2.41 wt%); Na_2O, K_2O, and TiO_2 concentrations are generally less than 0.2 wt%. The contents of Fe and P are relatively high, resulting in the ores being ferromanganese (Mn/Fe ≤ 1) and high-iron Mn-carbonate ores (Mn/Fe ≤ 3).

Samples of Mn-bearing limestones are characterized by lower Mn (0.75 to 8.92 wt%), Fe contents (6.78 to 38.21 wt%), and P contents (≤2.1 wt%). This translates into lower Mn/Fe_{auth} ratios (0.06 to 0.61) and P/Mn_{auth} ratios (0.003 to 0.377). The Mn_{EF} was elevated with values ranging from 28 to 1828 with a mean of 704. Conversely, the values of Fe_{EF} are relatively small, with a range of 6 to 113 and a mean of 43. Mean concentrations of other significant oxide concentrations within the Mn-bearing limestones are different from those of the Mn-carbonate ores, including SiO_2 (26.58 wt%), Al_2O_3 (4.30 wt%), CaO (9.11 wt%), and MgO (2.11 wt%); Na_2O, K_2O, and TiO_2 concentrations are generally less than 0.3 wt%.

The non-mineralized rocks of the middle member in the Talong Group have significantly lower Mn concentrations than the Mn-

Table 3
EMPA analytical results of kutnahorite, Fe-rhodochrosite, Mn-siderite, and Ca-rhodochrosite from the Zhuwuluke Mn carbonate ore deposit (wt%).

Kutnahorite

No.	MnO	FeO	CaO	MgO	SiO_2	Na_2O	Al_2O_3	CO_2	Total
ZWLK-18-1	8.88	7.53	29.06	8.94	0.00	0.04	0.00	40.00	94.45
ZWLK-18-2	9.10	7.30	28.31	9.70	0.00	0.00	0.00	39.97	94.38
ZWLK-18-3	11.62	9.58	29.02	5.70	0.00	0.00	0.21	40.37	96.50
ZWLK-18-4	16.66	9.52	26.93	3.64	0.00	0.01	0.00	40.17	96.93
ZWLK-18-5	15.72	9.06	28.62	3.07	0.00	0.04	0.05	40.21	96.77
ZWLK-18-6	16.90	8.42	27.67	3.18	0.00	0.00	0.05	39.87	96.09
ZWLK-18-7	15.68	9.17	27.37	4.22	0.00	0.01	0.01	40.15	96.61
ZWLK-18-8	16.58	9.10	27.78	3.34	0.00	0.00	0.00	40.29	97.09
ZWLK-18-9	17.95	9.27	25.76	3.08	1.05	0.00	0.00	38.41	95.52
ZWLK-18-10	16.41	9.62	25.96	0.14	0.10	0.00	0.14	38.90	91.27
ZWLK-8-1	11.97	10.99	25.72	5.81	0.00	0.00	0.00	38.91	93.40
ZWLK-8-2	12.12	11.18	26.62	5.89	0.00	0.00	0.00	39.89	95.70
ZWLK-8-3	12.52	13.61	25.97	4.44	0.15	0.01	0.10	39.83	96.63
ZWLK-8-4	10.91	13.26	25.38	4.91	1.91	0.00	0.00	36.76	93.13
ZWLK-8-5	10.26	14.58	25.85	6.59	1.44	0.00	0.00	39.31	98.03
ZWLK-8-6	11.28	14.58	26.30	5.21	0.00	0.00	0.00	40.65	98.02
ZWLK-8-7	12.13	14.70	25.14	4.91	0.00	0.00	0.00	40.11	96.99
ZWLK-8-8	12.52	14.16	25.70	5.12	0.00	0.00	0.00	40.63	98.13
ZWLK-8-9	12.14	13.89	25.99	4.62	0.00	0.03	0.00	40.08	96.75
ZWLK-8-10	12.62	13.88	25.76	4.66	0.00	0.02	0.00	40.21	97.15

Fe-rhodochrosite

No.	MnO	FeO	CaO	MgO	SiO_2	Na_2O	Al_2O_3	CO_2	Total
ZWLK-8-11	25.10	23.09	6.84	2.95	0.00	0.00	0.00	39.47	97.45
ZWLK-8-12	24.86	23.07	6.95	3.20	0.00	0.21	0.00	40.91	99.21
ZWLK-8-13	25.76	23.81	7.01	2.96	0.00	0.00	0.00	40.46	100.00
ZWLK-8-14	25.70	23.53	7.17	3.29	0.00	0.00	0.00	40.88	100.58
ZWLK-8-15	27.48	26.87	3.24	2.51	0.00	0.00	0.00	39.76	99.86
ZWLK-8-16	25.43	24.03	6.88	2.78	0.00	0.00	0.00	40.01	99.13
ZWLK-8-17	25.74	24.45	6.87	2.65	0.00	0.00	0.00	40.26	99.96
ZWLK-8-18	25.80	23.47	7.11	3.01	0.00	0.09	0.00	40.93	100.42
ZWLK-8-19	25.44	25.29	6.73	2.68	0.00	0.00	0.00	40.53	100.67
ZWLK-8-20	25.90	25.73	5.52	2.81	0.00	0.00	0.00	40.33	100.29
ZWLK-8-21	25.89	24.91	6.38	2.66	0.00	0.08	0.00	40.69	100.61
ZWLK-8-22	25.71	24.50	6.72	2.60	0.00	0.00	0.00	40.08	99.60
ZWLK-8-23	25.70	24.50	6.74	2.69	0.00	0.00	0.00	40.22	99.84

Mn-siderite

No.	MnO	FeO	CaO	MgO	SiO_2	Na_2O	Al_2O_3	CO_2	Total
ZWLK-8-24	21.03	33.53	2.91	2.37	1.27	0.00	0.00	38.15	99.26
ZWLK-8-25	22.61	29.47	4.34	3.90	0.00	0.00	0.00	41.28	101.59
ZWLK-26	21.99	27.88	4.30	3.92	0.00	0.00	0.00	39.93	98.03
ZWLK-8-27	20.16	33.91	3.28	3.29	0.01	0.00	0.00	40.71	101.36
ZWLK-8-28	21.97	32.54	3.49	2.61	0.38	0.00	0.00	39.77	100.77
ZWLK-8-29	19.80	31.15	7.85	2.35	0.76	0.00	0.00	40.23	102.13
ZWLK-8-30	22.90	31.53	2.87	2.92	0.32	0.00	0.00	39.78	100.33
ZWLK-8-31	21.47	28.53	5.26	2.89	1.69	0.06	0.00	37.91	97.80
ZWLK-8-32	24.23	28.86	3.81	3.98	0.33	0.07	0.28	38.52	100.08
ZWLK-8-33	21.86	34.50	2.66	2.97	0.60	0.01	0.00	38.46	101.06
ZWLK-8-34	21.32	32.94	3.25	2.90	0.46	0.00	0.07	37.70	98.64
ZWLK-8-35	19.23	33.01	2.14	6.26	0.10	0.00	0.00	38.57	99.31

Ca-rhodochrosite

No.	MnO	FeO	CaO	MgO	SiO_2	Na_2O	Al_2O_3	CO_2	Total
ZWLK-18-11	33.60	6.36	13.06	2.86	1.93	0.04	0.95	35.37	94.17
ZWLK-18-12	32.17	8.68	14.28	3.86	2.38	0.11	1.98	37.41	100.86

Notes: The CO_2 was calculated by content of $MnCO_3$, $FeCO_3$, $CaCO_3$, $MgCO_3$, and Al_2CO_3.

carbonate ores (Table 4). They have Mn contents of 0.04 to 0.2 wt%, with Mn_{EF} values ranging from 1.31 to 36.54. The Fe_2O_3 contents (2.06 to 5.71 wt%) and values of Fe_{EF} (1.71 to 5.06) were lower than those in the Mn-carbonate ores. Other oxide abundances within the non-mineralized rocks are different from those of the Mn-carbonate ores and Mn-bearing carbonates to a degree. For instance, SiO_2, Al_2O_3, Na_2O, and K_2O are higher (61.87 to 90.67, 2.37 to 19.40 wt%, 0.11 to 2.19 wt %, and 0.28. wt % to 3.29 wt%, respectively), while the CaO content is lower (0.16 to 4.72 wt%).

5.2. Trace and rare earth elements

Except for some transition metals, such as Li (mean = 43.20 and 73.75 ppm for Mn-carbonate ores and Mn-bearing carbonates, respectively. The same as below.), V (mean = 38.32 and 50.40 ppm), Cr (mean = 55.18 and 62.34 ppm), Co (mean = 38.84 and 26.16 ppm), Ni

Ore Minerals	Sedimentary-diagenetic period	Hydrothermal period	Supergenetic oxidation period
Ankerite	—		
Ca-rhodochrosite	—		
Mn-siderite	—		
Pyrite	—		
Fe-rhodochrosite	—		
Rhodochrosite	—	—	
Siderite	—		
(Fe-, Mn-bearing) dolomite	—		
Kutnahorite	—	—	
Mn-calcite	—	—	
Quartz	—	—	
Fe-calcite		—	
Mn, Fe oxide			—
Chlorite			—
Malachite			—

Fig. 5. Metallogenetic periods and related mineral assemblage of the Zhuwuluke manganese deposit.

(mean = 38.42 and 44. 06 ppm), Cu (mean = 89.28 and 286.33 ppm), Zn (mean = 177.44 and 103.15 ppm), Sr (mean = 262.00 and 147.00 ppm), Ba (mean = 365.86 and 95.39 ppm), Ce (mean = 25.56 and 28.84 ppm), Y (mean = 28.20 and 23. 00 ppm), and Pb (mean = 98.52 and 61.65 ppm), most trace elements in the Mn-carbonate ores and Mn-bearing carbonates are present at low concentrations (<20 ppm, Table 4). The incompatible elements Hf, Th, and Sc have mean concentrations of 0.47, 1.87, and 3.56 and 1.00, 3.85, and 5.25 ppm for Mn-carbonate ores and Mn-bearing carbonates, respectively. Zirconium is present at a relatively higher concentration in the Mn-carbonate ores and Mn-bearing carbonates, ranging from 13.1 to 19.3 ppm and 11.5 to 94.6 ppm, respectively. A positive correlation between Zr and Al_2O_3 (R^2 = 0.78) is also present within the Mn-rich chemical precipitates. Most of the wall-rock samples have higher transition metal concentrations (e.g., V > 50 ppm, Cr > 100 ppm) and incompatible elements (e.g., Sc > 3 ppm, Rb > 18 ppm, Zr > 50 ppm, Ba > 70 ppm, Hf > 1 ppm, Th > 3 ppm) than the Mn-carbonate ores. In contrast, the non-mineralized rocks are also marked by lower Sr contents, ranging from 37.4 to 157 ppm.

The Mn ores, Mn-bearing limestones, and associated wall rocks show significant differences in their REE + Y concentrations and post-Archean average Australian shale (PAAS)-normalized patterns (Fig. 9). Samples of the Mn-carbonate ore and Mn-bearing limestone are depleted in REE + Y (ΣREE + Y contents range from 87.08 to 126.02 ppm and 33.38–253.67 ppm, with means of 107.13 and 103.67 ppm, respectively). The REE + Y distribution of Mn-carbonate ores deviates from that of PAAS by displaying negative Ce anomalies (δCe = 0.87 ± 0.10) and positive Y anomalies (δY = 1.30 ± 0.13). In contrast, some Mn-bearing carbonates show negative Ce anomalies (δCe = 0.99 ± 0.22) and positive Y anomalies (δY = 1.06 ± 0.43), while others display positive Ce anomalies (δCe = 1.08 ± 0.08) and weakly negative Y anomalies (δY = 1.17 ± 0.33). Slight fractionations between light and heavy REEs (Nd/Yb_{PAAS} = 0.69 ± 0.16 and 0.65 ± 0.20, respectively) for Mn-carbonate ores and Mn-bearing carbonates are apparent (Fig. 7a). A distinct positive Eu anomaly characterizes all Mn-carbonate ore and Mn-bearing carbonate samples (δEu = 4.32 ± 1.15 and 2.03 ± 1.43, respectively), unlike those of wall-rock samples (δEu = 1.07 ± 0.18). Moreover, all analyzed Mn-carbonate ores and Mn-bearing carbonates have subchondritic Y/Ho ratios ranging from 35.08 to 38.34 and 25.00–43.02, respectively, falling between those of Mn oxides and seawater (25 to 36) on the whole.

Generally, the REE + Y concentrations of the wall rocks are higher

than those of Mn-carbonate ores and Mn-bearing carbonates (ΣREE + Y from 49.06 to 289.29 ppm, with a mean of 161.15 ppm). The wall rocks display relatively uniform PAAS-normalized REE + Y patterns, without distinct light REE depletion (Nd/Yb_{PAAS} = 0.97 ± 0.25) or Ce anomalies of 1.02 ± 0.06 (Fig. 7c). Half of the samples have no Eu anomalies except two sandstone samples showing positive Eu anomalies and one carbonaceous siltstone displaying a weakly negative Eu anomaly. Weakly negative Y anomalies of carbonaceous siltstone and sandstone are observed, and wall-rock samples show Y/Ho ratios ranging from 23.31 to 28.84.

5.3. Organic carbon, inorganic carbon, and oxygen isotopic compositions

The total organic carbon (TOC) of the Mn-carbonate ores and associated wall rocks, as well as the carbon isotopic ratios for organic carbon from selected samples, are presented in Table 5 and Fig. 6. The Mn-carbonate ores and Mn-bearing limestones generally have low TOC abundances that varying from 0.12 to 0.31 wt%, with a mean of 0.19 wt%, and average TOC for wall-rock sample is 0.23 wt%.

The $δ^{13}C_{org}$ compositions of the Mn-carbonate ores and Mn-bearing limestones are relatively uniform, varying from −26.77 to −22.53‰, with a mean of −25.31‰. The $δ^{13}C_{carb}$ values of Mn-carbonate ores ranged from −16.53‰ to −8.81‰, with a mean of −10.92‰. Additionally, the $δ^{18}O_{carb}$ values of Mn-carbonate ores ranged between −12.60 ‰ and −4.65‰, with a mean of −8.99‰.

5.4. Sulfur isotopic compositions

The sulfur contents in Mn-carbonate ores, Mn-bearing limestones, and wall rocks are reported in Table 4. Pyrite is the primary sulfide within Mn-bearing limestones. Most Mn-carbonate ores are characterized by low sulfur contents, less than or equal to 1.93 wt%, while the Mn-bearing limestones have higher concentrations, with a mean of 2.88 wt% and a range from 0.14 to 12.43 wt%. The wall rocks have much lower sulfur contents, ranging from 0.04 to 0.29 wt%, with a mean of 0.12 wt%. Pyrite grains from three Mn-bearing carbonate samples yielded $δ^{34}S$ values from − 25.29 to − 3.01‰, with a mean of −10.16‰. Regarding eight Mn-bearing carbonate and one Mn ore sample, except two samples ($δ^{34}S$ = 3.25‰ and 1.56‰), others range from −21.97 to −1.50‰, with a mean of −9.9‰ (Table 6, Fig. 8).

6. Discussion

6.1. Depositional environment

In the Middle Devonian, a new extensional environment occurred north of the Aoyitage-Kuerliang Paleozoic rift and the Kushanhe basin leading to a unit of transgression sequence (Zhang et al., 2021). Lithological evidence, including dark gray color, well-developed horizontal bedding, and abundant organic matter, suggests that the rocks of the Talong Group was deposited in a relatively stable environment. Moreover, the disappearance of fossils supports that the rocks of the Talong Group were deposited under hemipelagic conditions. A stable sedimentary environment with a low sedimentation rate is necessary for a large manganese ore deposit (Zhang et al., 2020b). In the Early Carboniferous, the Kushanhe Basin had been closed. As a result, the accumulation of Mn at Zhuwuluke is located margin of the restricted basin.

Sedimentary pyrite is generally formed in anoxic environments, and the availability of Fe^{2+} in addition to HS^- determines the size distribution and morphology of pyrite. Thus, pyrite in sedimentary rocks has been widely used to infer paleoredox conditions (Wilkin et al., 1996). The size of early diagenetic pyrite is generally large because of the extension within sediments (Wilkin et al., 1997). Pyrite grains in the Mn-bearing limestone samples are generally euhedral and confined to laminae and consistent with an early diagenetic origin driven by

Table 4
Major (%) and trace element (10^{-6}) compositions of Mn-carbonate ores, Mn-bearing limestones and wall rocks at Zhuwuluke mine.

Sample	Z-1	Z-2	Z-3	Z-4	Z-5	Z-6	Z-7	Z-8	Z-9	Z-10	Z-11	Z-12	Z-13	Z-14	Z-15
Type	Sa.	M. l.	M. l.	M. l.	Mn ore	M. l.	M. l.	Mn ore	M. l.	Si.	M. l.	M. l.	M. l.	M. l.	Mn ore
SiO_2	81.44	12.66	21.92	39.39	18.41	11.39	44.25	7.90	35.78	70.06	45.09	16.27	17.80	15.13	17.15
Al_2O_3	4.53	3.78	3.51	4.22	1.66	2.35	9.12	1.51	4.40	15.58	2.51	3.93	3.18	2.84	2.18
Fe	1.77	24.60	18.07	9.78	8.86	35.41	6.78	11.37	11.61	4.04	9.94	26.25	19.22	25.81	10.81
MgO	0.45	3.80	3.68	3.56	2.92	3.02	3.05	2.70	3.01	1.47	4.04	4.50	3.47	4.77	2.97
CaO	4.72	5.29	12.81	13.29	18.59	1.07	9.92	16.03	13.29	0.19	12.82	4.91	12.18	4.39	18.22
Na_2O	0.85	<mdl	0.16	0.48	<mdl	<mdl	0.25	0.18	<mdl	1.19	<mdl	0.05	0.04	0.05	0.04
K_2O	0.57	0.20	<mdl	0.28	0.16	<mdl	1.27	0.22	0.23	2.00	<mdl	0.00	0.02	0.01	0.07
Mn	0.08	8.82	4.49	3.61	11.90	5.76	4.14	16.59	5.02	0.07	1.12	5.47	5.78	6.74	10.11
P	0.01	0.09	0.14	0.03	1.20	0.02	0.01	1.19	0.11	0.02	0.03	0.08	1.33	0.19	2.10
TiO_2	0.44	0.34	0.60	0.20	0.21	0.25	0.54	0.06	0.15	0.57	0.17	0.14	0.12	0.08	0.06
SO_3	0.04	<mdl	4.26	0.70	<mdl	0.22	<mdl	<mdl	0.69	0.12	1.26	5.10	9.95	0.15	1.93
LOI	4.69	26.89	20.56	18.88	24.39	23.55	16.29	27.97	18.62	3.78	18.12	26.21	24.09	27.10	25.27
Mn/Fe	0.05	0.36	0.25	0.37	1.34	0.16	0.61	1.46	0.43	0.02	0.11	0.21	0.30	0.26	0.94
Mn_{EF}	8.20	1036.15	567.23	379.72	3181.79	1088.66	201.72	4877.88	506.42	1.96	197.28	618.49	806.58	1052.48	2056.09
P/Mn	0.15	0.01	0.03	0.01	0.10	0.00	0.00	0.07	0.02	0.27	0.03	0.02	0.23	0.03	0.21
Li	13.2	45.8	57.6	46.5	18.7	29	55.7	9.72	64.7	77.2	37.1	49.1	43.1	53.1	44.8
Be	0.496	1.83	0.505	0.537	2.01	1.08	2.42	2.78	0.785	1.9	0.186	1.01	1.08	1.26	1.55
Sc	4.05	4.92	4.84	7.16	3.29	3.21	10.8	2.55	6.54	25.2	4.69	4.6	3.5	3.79	3.04
Ni	15.5	24.8	32	39	25.2	8.55	92.5	24.5	35.7	74.3	13.3	47.6	50.3	19	41.3
U	1.19	1.47	1.59	1.09	9.09	0.819	2.18	6.18	2.6	2.36	0.955	0.474	5.73	2.76	10.7
V	44.3	54.2	42.8	46.3	41.1	27.2	97.9	48.7	55.8	160	27.1	31.2	38.1	29.9	37
Cr	314	38.3	35.1	48.6	42.6	24.2	71.2	17.3	50	186	119	42.8	46.9	25.5	33.3
Co	5.22	26.9	29.6	20.6	32.8	3.46	21.8	41.7	28.1	11.2	5.36	20.1	38.5	6.9	41.7
Cu	9.79	27.2	277	392	39.9	24	257	31.4	134	36.1	7.14	214	294	57.9	98.7
Zn	22.6	162	124	70.9	83.5	79.4	87.1	117	89.2	65.3	38	106	95	72.9	80.7
Ga	5.41	9.42	8.19	8.59	8.64	6.73	14.2	10.1	9.22	18.7	3.95	16.8	16.5	17.7	22.7
Ge	0.891	0.757	0.868	0.905	0.501	0.724	1.18	0.332	1.12	1.53	0.977	1.37	1.01	1.39	0.698
As	1.31	0.867	18.6	4.02	11.4	1.77	7.38	12	5.74	24.3	4.14	22.8	60.6	1.85	35.5
Rb	28.6	14.8	1.59	20.1	12.3	0.648	89.1	15.8	17.5	94.6	0.417	1	1.97	0.183	4.77
Sr	105	76	183	212	291	42.1	240	276	241	157	112	62.1	191	58.5	281
Y	10.7	19.1	17.3	13.8	31.2	8.56	25.7	20.5	29.1	22.6	14.4	10.7	23.9	12.4	23.4
Zr	166	33.1	20.9	28.7	19.3	20.3	85	17.4	36.5	97.3	58.9	28.4	29.1	18.9	18.9
Nb	7.77	3.57	2.01	2.84	1.69	2.11	8.34	1.7	3.44	11.7	3.33	3.52	3.33	2.04	1.8
Mo	22.1	1.45	5.49	7.01	4.16	0.841	1.01	2.4	2.69	2.89	7.35	2.05	3.64	2.16	4.08
Ag	0.199	0.33	0.13	0.153	0.091	0.069	0.172	0.108	0.252	0.41	0.087	0.112	0.106	0.045	0.092
Cd	0.102	0.584	0.496	0.279	0.622	0.098	0.381	0.922	0.367	0.09	0.291	0.27	0.29	0.097	0.37
In	0.016	0.16	0.146	0.071	0.038	0.018	0.057	0.031	0.048	0.058	0.387	0.035	0.036	0.046	0.039
Sn	0.981	1.06	0.755	1.04	0.94	0.777	2.15	0.825	1.13	2.69	0.406	0.404	0.38	0.409	0.437
Sb	0.396	0.18	0.453	0.632	0.371	0.111	0.211	0.272	0.43	1.05	0.336	0.424	1	0.307	0.403
Cs	0.989	0.827	0.234	1.13	0.548	0.342	4.25	0.736	1.55	6.8	0.089	0.183	0.152	0.068	0.344
Ba	99.1	79	101	66.6	44.7	9.91	369	58	50.5	361	665	16.2	14.1	7.36	25.6
La	16.1	11.6	7.37	8.54	18.4	6.29	27	13.8	20.7	30.6	11.8	9.3	14.9	14.6	16.4
Ce	31.9	24.3	17.8	19.1	30.3	12.9	47	23	36.4	66.4	23.3	18.5	24.5	20.9	25.8
Pr	3.51	2.56	1.86	1.9	3.68	1.37	5.59	2.7	4.38	6.53	2.6	1.95	2.88	2.7	3.22
Nd	13.3	11	8.79	7.99	15.8	5.16	22	10.9	18.6	25.2	10.6	7.87	12	11	13.6
Sm	2.49	3.31	3.24	2.43	4.3	1.14	5.22	2.65	4.87	5.32	2.3	2.17	3.19	2.42	3.68
Eu	0.6	1.17	1.61	0.983	3.7	0.407	1.19	3.38	1.63	1.07	0.834	0.782	2.32	0.829	3.37
Gd	2.04	4.29	4.25	3.11	5.44	1.12	5.33	3.2	5.71	4.86	2.33	2.24	4.16	2.48	5.01
Tb	0.309	0.65	0.619	0.485	0.785	0.196	0.824	0.489	0.88	0.684	0.36	0.316	0.582	0.348	0.675
Dy	1.81	3.44	3.39	2.86	4.4	1.32	4.75	2.82	5.17	4.38	2.1	1.86	3.53	1.99	3.77
Ho	0.371	0.623	0.632	0.529	0.848	0.297	0.934	0.552	0.999	0.831	0.425	0.363	0.696	0.39	0.667
Er	1.07	1.59	1.61	1.32	2.17	0.887	2.56	1.45	2.58	2.21	1.14	1.02	1.85	1.04	1.64
Tm	0.164	0.22	0.221	0.18	0.278	0.132	0.376	0.198	0.354	0.307	0.16	0.155	0.269	0.15	0.219

Table 4 (*continued*)

Sample	Z-1	Z-2	Z-3	Z-4	Z-5	Z-6	Z-7	Z-8	Z-9	Z-10	Z-11	Z-12	Z-13	Z-14	Z-15
Yb	1.16	1.48	1.45	1.19	1.71	0.889	2.58	1.25	2.25	2.04	1.09	1.04	1.74	0.986	1.38
Lu	0.18	0.227	0.226	0.174	0.256	0.137	0.402	0.188	0.334	0.314	0.16	0.165	0.278	0.152	0.207
Hf	4.2	0.947	0.636	0.827	0.48	0.591	2.48	0.476	1.05	2.57	1.52	0.806	0.752	0.485	0.433
Ta	0.598	0.289	0.189	0.236	0.141	0.19	0.621	0.158	0.279	0.736	0.269	0.265	0.23	0.155	0.137
W	1.63	0.752	0.891	0.917	0.594	0.495	1.87	0.586	0.842	2.02	0.925	0.596	0.699	1.09	0.489
Tl	0.115	0.059	0.009	0.08	0.048	0.006	0.351	0.061	0.067	0.456	0.006	0.009	0.014	0.001	0.025
Pb	9.86	120	72.9	43	154	3.61	5.28	92.3	104	19.5	5.41	86.9	73	4.45	62.3
Bi	0.055	0.357	1.18	0.845	0.359	0.086	0.145	0.414	0.773	0.653	0.046	0.328	0.95	0.099	0.907
Th	4.69	4.01	2.71	3.45	1.79	2.44	9.79	1.82	4.09	11.9	2.56	3.1	2.67	1.67	1.46
ΣREE	75.00	66.46	53.07	50.79	92.07	32.25	125.76	66.58	104.86	150.75	59.20	47.73	72.90	59.99	79.64
δEu	1.25	1.46	2.04	1.68	3.60	1.70	1.06	5.47	1.46	0.99	1.70	1.67	3.00	1.59	3.70
δCe	0.98	1.03	1.11	1.09	0.85	1.01	0.88	0.87	0.88	1.08	0.97	1.00	0.86	0.77	0.82
δY	1.04	1.04	0.94	0.89	1.29	1.09	0.97	1.31	1.02	0.94	1.22	1.04	1.22	1.12	1.17
ΣREE + Y	85.70	85.56	70.37	64.59	123.27	40.81	151.46	87.08	133.96	173.35	73.60	58.43	96.80	72.39	103.04
Y/Ho	28.84	30.66	27.37	26.09	36.79	28.82	27.52	37.14	29.13	27.20	33.88	29.48	34.34	31.79	35.08

Sample	Z-16	Z-17	Z-18	Z-19	Z-20	Z-21	Z-22	Z-23	Z-24	Z-25	Z-26	Z-27	Z-28	Z-29	Z-30	Z-31
Type	M. l.	M. l.	Mn ore	Sa.	M. l.	M. l.	Mn ore	M. l.	M. l.	M. l.	M. l.	M. l.	M. l.	Sa.	Shale	Sa.
SiO$_2$	21.00	19.22	36.83	90.67	12.85	59.63	7.62	21.60	31.17	35.53	18.19	26.14	26.55	74.54	67.25	61.87
Al$_2$O$_3$	1.66	3.73	2.42	2.37	3.99	11.88	1.82	4.99	3.07	1.86	3.29	4.51	7.19	10.94	16.27	19.40
Fe	18.94	29.60	18.33	1.60	14.84	13.39	19.36	26.34	14.95	14.58	38.21	11.46	12.75	3.03	4.38	4.44
MgO	3.09	4.10	1.19	0.55	4.76	3.19	2.28	3.73	1.67	1.39	2.19	4.79	3.80	1.50	1.73	2.11
CaO	12.06	1.24	5.95	1.43	15.02	0.27	12.84	7.27	12.50	11.07	2.13	15.75	14.82	1.20	0.16	0.25
Na$_2$O	0.04	0.06	0.05	0.11	0.04	0.35	0.06	0.08	0.04	0.04	0.06	0.03	0.01	2.19	1.76	1.82
K$_2$O	0.00	0.00	0.11	0.28	0.13	0.35	0.09	0.09	0.11	0.03	0.03	0.00	0.11	1.73	2.44	3.29
Mn	5.39	5.35	10.09	0.20	8.92	0.75	12.04	3.30	8.00	7.68	3.38	5.11	4.83	0.04	0.09	0.06
P	2.03	0.14	1.25	0.01	0.46	0.02	2.62	0.22	1.89	1.28	0.06	0.04	1.36	0.02	0.02	0.02
TiO$_2$	0.06	0.12	0.06	0.14	0.11	0.56	0.08	0.17	0.10	0.05	0.12	0.14	0.24	0.56	0.69	0.94
SO$_3$	1.51	0.17	0.26	<mdl	0.25	0.31	0.38	12.43	0.14	0.63	11.88	0.41	1.83	0.29	<mdl	0.04
LOI	23.63	23.90	10.30	2.18	28.55	5.18	24.68	22.98	14.49	14.98	20.19	25.05	19.39	3.67	3.48	4.61
Mn/Fe	0.28	0.18	0.55	0.12	0.60	0.06	0.62	0.13	0.54	0.53	0.09	0.45	0.38	0.01	0.02	0.01
Mn$_{EF}$	1439.49	637.70	1849.73	36.56	991.26	27.85	2937.05	293.63	1156.93	1829.37	455.49	503.50	298.20	1.73	2.39	1.31
P/Mn	0.38	0.03	0.12	0.04	0.05	0.02	0.22	0.07	0.24	0.17	0.02	0.01	0.28	0.46	0.22	0.43
Li	48.4	232	93.1	122	52.5	143	49.7	64.4	41.6	134	57.7	70.7	149	26.3	66.5	88.9
Be	0.988	1.44	1.03	0.378	1.05	0.691	1.77	0.853	1.06	1.33	2.05	0.859	1.06	2.25	2.74	4.86
Sc	2.1	13.5	6.45	2.36	10.6	9.13	2.48	3.21	2.63	1.94	1.98	2.34	3.57	5.8	15.7	10.2
Ni	25.8	32.5	61.6	21.1	75.6	102	39.5	47.9	50.6	49	14.8	54.8	65.5	37	58	48.5
U	3.68	0.728	3.15	1.22	1.95	4.87	7.4	1.32	3.63	1.85	0.564	0.872	6.44	1.89	3.79	4.73
V	28.9	75.9	36.8	38.5	73.4	125	28	48.8	44.6	18.6	28.6	27.6	86	62.8	159	155
Cr	41.3	80.9	151	312	46.7	247	31.7	58.9	25.7	74.7	72.7	33.7	63.5	188	120	147
Co	9.88	11.3	49	8.09	74.3	22.2	29	34.8	39.6	36.2	10.5	35.9	47.2	11.3	10.7	11.8
Cu	119	299	233	39.2	457	895	43.4	410	95.7	88.7	193	878	607	18.3	55.8	431
Zn	50	117	466	45.2	93.2	175	140	118	109	69.1	86.1	98	223	61.9	79.1	108
Ga	14.5	89	36.7	2.91	40.2	20	33.9	14.6	20.1	16.3	10.9	14.8	19.2	12.1	21.5	23.7
Ge	1.03	5.13	1.39	1.09	1.7	2.34	0.996	1.45	1.01	0.939	1.61	1.24	1.67	1.07	1.53	1.76
As	8.95	2.02	15.3	2.17	38.9	2.96	8.53	44.7	48.2	42.1	37.8	52.9	21.2	10.1	15.7	14.1
Rb	0.833	0.708	5.18	18.6	7.52	19.1	5.83	3.92	7.24	2.99	0.961	1.11	6.1	68	155	150
Sr	219	38.8	231	37.4	197	36.3	231	97.4	216	204	51.7	168	294	77.9	128	156
Y	35.8	6.84	27.3	7.92	30.1	18.9	38.6	24.8	65.5	25.7	8.87	19.6	49	12.1	27.9	32.4
Zr	17.5	25.5	13.1	52.7	26.4	94.6	18.2	27	25.4	11.5	17.8	35.4	47	120	155	207
Nb	1.89	3.3	1.49	2.96	3.01	13.1	2.12	3.54	2.76	1.39	2.12	3.98	5.66	10.7	15.4	21
Mo	4.06	2.04	12.4	24.6	2.97	13	2.98	3.49	2.67	8.44	6.2	1.3	8.06	9.33	2.25	4.14
Ag	0.063	0.164	0.048	0.068	0.337	0.442	0.128	0.158	0.104	0.066	0.126	0.177	0.272	0.287	0.298	0.564
Cd	0.176	0.142	3.96	0.351	0.291	0.202	0.531	0.353	0.269	0.319	0.188	0.368	0.666	0.163	0.168	0.339
In	0.031	0.029	0.332	0.039	0.244	0.071	0.106	0.054	0.065	0.18	0.035	0.037	0.059	0.037	0.069	0.073

Table 4 (*continued*)

Sample	Z-16	Z-17	Z-18	Z-19	Z-20	Z-21	Z-22	Z-23	Z-24	Z-25	Z-26	Z-27	Z-28	Z-29	Z-30	Z-31
Sn	0.259	0.334	0.347	0.595	0.645	1.72	0.538	0.499	0.674	0.496	0.33	0.737	0.945	1.74	2.86	3.69
Sb	0.481	0.194	0.606	0.395	0.609	1.7	0.801	1.06	0.498	0.92	1.37	0.34	1.06	0.877	0.473	0.749
Cs	0.146	0.077	1.01	1.87	0.469	1.56	0.461	0.363	0.548	0.453	0.271	0.104	0.492	3.5	7.84	11.4
Ba	11.2	9.17	1544	78.2	32.5	76.6	157	108	43.9	32.3	35	15.4	165	395	641	811
La	15.7	5.43	12.1	8.69	11.1	25.8	14	11.6	24	9.79	6.61	13.3	35.2	24.6	45.4	54.4
Ce	27.1	10.9	20.3	16.9	21.7	53.2	28.4	24.9	60.7	18.7	16.3	30.4	68.1	50.1	92.4	107
Pr	2.98	1.02	2.64	1.79	2.51	5.53	3.24	2.85	6.69	2.51	1.62	3.05	7.44	5.55	9.81	12.2
Nd	12.5	4.1	13.1	6.74	11.1	20.1	15.8	13.9	32.7	13.1	7.05	12.7	32.9	21.3	36.8	46.9
Sm	3.08	1.15	3.57	1.37	3.6	4.28	4.35	4.78	10.3	4.08	2.1	3.32	8.73	3.83	6.92	8.48
Eu	2.67	0.354	4.1	0.339	1.6	0.877	3.99	1.96	6.3	2.91	0.628	1.06	3.65	0.753	1.37	1.51
Gd	4.29	1.36	4.6	1.45	4.97	3.44	5.34	7.47	15.6	5.1	2.26	4.36	11.9	3.16	6.05	7.61
Tb	0.63	0.169	0.615	0.239	0.71	0.568	0.734	1.03	2.23	0.702	0.318	0.671	1.66	0.472	0.953	1.18
Dy	4.27	0.84	3.75	1.49	4.34	3.43	4.81	5.75	14	4.32	1.87	4.12	10.1	2.74	5.55	7.23
Ho	0.924	0.159	0.712	0.303	0.849	0.652	1.03	0.95	2.62	0.829	0.342	0.732	1.91	0.506	1.1	1.39
Er	2.43	0.414	1.73	0.817	2.1	1.91	2.69	2.14	6.38	2.04	0.942	1.82	4.74	1.42	3.08	3.85
Tm	0.331	0.065	0.223	0.117	0.312	0.299	0.39	0.308	0.884	0.283	0.144	0.278	0.673	0.215	0.431	0.596
Yb	1.97	0.498	1.28	0.780	2.04	2.03	2.31	1.93	5.05	1.63	0.959	1.74	3.92	1.45	2.91	3.97
Lu	0.306	0.08	0.215	0.112	0.323	0.321	0.335	0.28	0.718	0.245	0.142	0.255	0.568	0.209	0.421	0.573
Hf	0.481	0.408	0.395	1.64	0.665	2.72	0.564	0.928	0.915	0.411	0.537	1.25	1.56	3.72	4.56	6.38
Ta	0.133	0.12	0.115	0.247	0.192	0.79	0.17	0.275	0.244	0.121	0.168	0.376	0.474	0.898	1.14	1.55
W	0.537	0.369	0.772	2.32	2.59	2.48	0.829	1.13	0.661	0.813	0.837	0.802	1.26	1.94	2.87	3.45
Tl	0.002	0.005	0.034	0.090	0.029	0.099	0.031	0.029	0.041	0.054	0.009	0.01	0.05	0.377	0.64	0.872
Pb	24.5	43.3	149	15.7	161	45.4	35	100	26	78.7	60.4	22.1	153	14.8	19.8	16.7
Bi	0.289	0.051	0.208	0.052	1.06	0.375	0.288	0.743	0.109	0.12	0.362	1.14	4.22	0.186	1.7	1.11
Th	1.49	2.12	2.08	3.33	2.21	12.5	2.19	3.61	2.87	1.62	2.44	5.2	6.47	9.28	16.5	21.4
ΣREE	79.18	26.54	68.94	41.14	67.25	122.44	87.42	79.85	188.17	66.24	41.29	77.81	191.49	116.31	213.20	256.89
δEu	3.46	1.33	4.76	1.13	1.78	1.08	3.90	1.54	2.34	3.00	1.36	1.31	1.69	1.02	1.00	0.89
δCe	0.91	1.07	0.83	0.99	0.95	1.03	0.97	1.00	1.11	0.87	1.15	1.10	0.97	0.99	1.01	0.96
δY	1.44	1.49	1.33	0.94	1.25	1.01	1.38	0.84	0.86	1.08	0.88	0.90	0.89	0.82	0.90	0.81
ΣREE+Y	114.98	33.38	96.24	49.06	97.35	141.34	126.02	104.65	253.67	91.94	50.16	97.41	240.49	128.41	241.10	289.29
Y/Ho	38.74	43.02	38.34	26.14	35.45	28.99	37.48	26.11	25.00	31.00	25.94	26.78	25.65	23.91	25.36	23.31

Notes: δCe = [Ce/√(2/La*Pr)]$_{PAAS}$; δEu = [Eu/√(Sm*Gd)]$_{PAAS}$; δY = [2Y/(Dy + Ho)]$_{PAAS.}$ mdl = minimum detection limit.

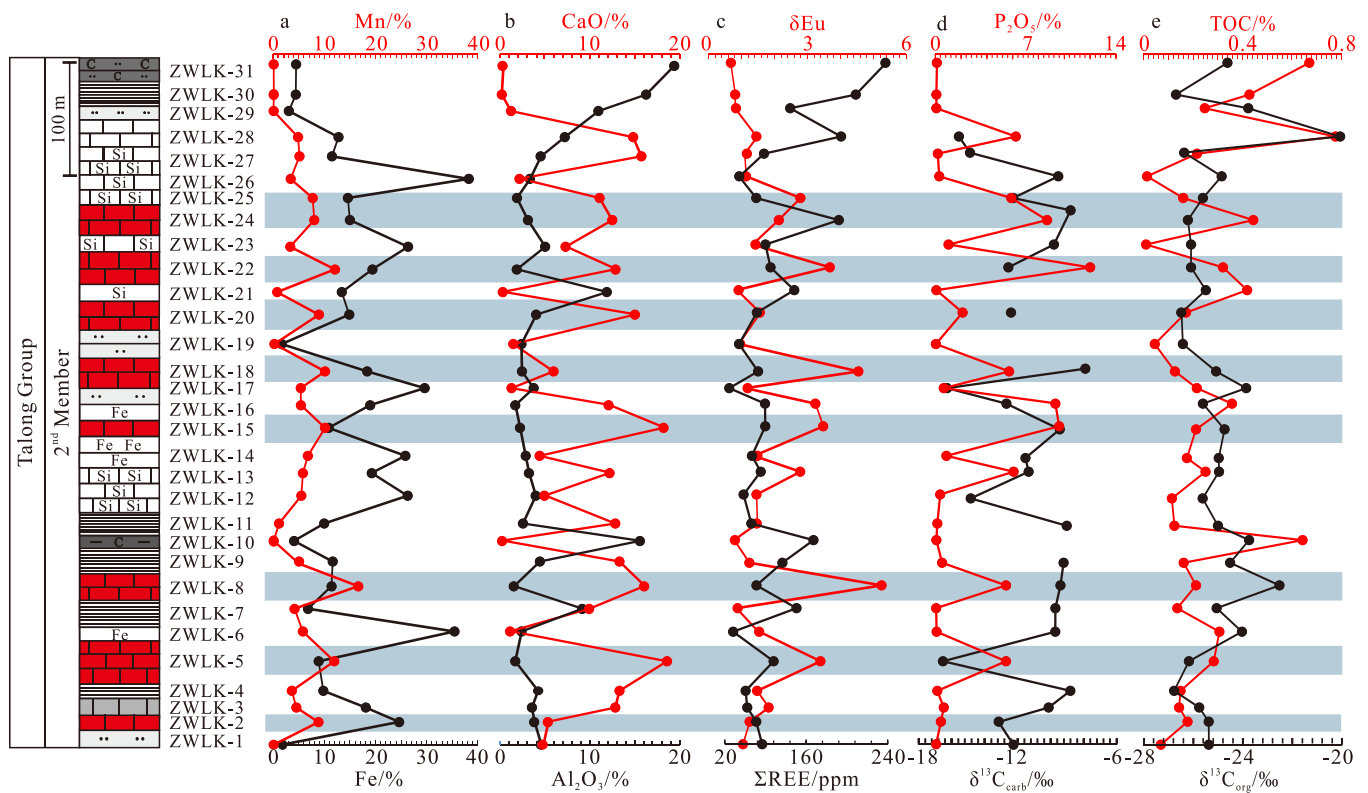Abbreviations: Z. = ZWLK; Sa. = Sandstone; M. l. = Mn-bearing limestone; Si. = Siltstone; EF = enrichment factor.

Fig. 6. Stratigraphic distributions of selected major elements, trace element, and carbon isotopic compositions for the rocks of 2nd Member of the Lower Carboniferous Talong Group.

microbial sulfate reduction (Wilkin et al., 1996). The low $\delta^{34}S$ values of pyrite grains and Mn-bearing carbonates at Zhuwuluke (-25.29 to −3.01‰ and −21.97 to −1.50‰, respectively) are different from those of Dawu manganese ore deposit in South China (Fig. 8b, Wu et al., 2016), but they are similar to those from the Ortokarnash manganese deposit (Table 6, Fig. 8a, Zhang et al., 2020), which are consistent with microbially mediated diagenetic sulfate reduction (Strauss, 1999). The sulfur isotopic compositions can be attributed to the sulfate supply from the upper water in the BSR beginning. Moreover, the bulk $\delta^{34}S$ compositions of two Mn-bearing limestone samples with high Ba contents are positive (Table 6), which were probably influenced by barite, because ^{34}S is preferentially enriched in sulfate radicals (Garrels and Lerman, 1984).

The REE + Y pattern of marine carbonate is typically used as a proxy for paleoseawater geochemistry and redox conditions. Although terrigenous contamination has the ability to affect Ce anomalies, it is relatively weak given that there is no meaningful correlation between δCe and Al_2O_3 ($R^2 = 0.05$). Typically, soluble Ce^{3+} tends to be absorbed onto ferromanganese oxides and was oxided to Ce^{4+} (Bau and Koschinsky, 2009). The PAAS-normalized REE + Y patterns of most analyzed wall-rock samples are different from those of modern seawater (LREE depletion and negative Ce anomalies). Under reducing water conditions, seawater is characterized by weakly negative or positive Ce anomalies (Sholkovitz et al., 1994; Bau and Koschinsky, 2009). Moreover, the degree of the Ce anomaly is related to the sedimentary velocity. Hydrogenic Fe–Mn crust formed at low velocity usually shows a mostly positive Ce anomaly. In contrast, the crust formed rapidly displays a slightly negative Ce anomaly. Additionally, a low oxygen content can also restrict the large-scaled migration of Ce^{4+} compounds. Slightly negative Ce anomalies are also likely to be related to local redox conditions, and/or some reactions occurred after sedimentation (Bau and Koschinsky, 2009). However, the Mn-rich samples at Zhuwuluke show no marked Ce anomalies (Fig. 7a). Therefore, it can be speculated that the Mn-carbonate ores and Mn-bearing limestones in the 2nd Member of

the Talong Group were probably deposited under rapid oxidation conditions.

In general, Y and Ho always occur together during geochemical progress owing to their similar charge and ionic radii. Most of the analyzed wall rock and some Mn-poor limestone samples show Y/Ho ratios ranging from 23.31 to 29.48, which are close to that of PAAS (27.25, MeLennan, 1989). The average of Y/Ho ratios for manganese carbonate ore samples is 34.49, which can be attributed to the Fe-Mn oxides adsorption (Bau et al., 2014). However, the Mn-carbonate ores and Mn-bearing limestones with negative Ce anomalies display positive Y anomalies, which may suggest that the Mn-(oxyhydr)oxides deposited rapidly from the water column, because REE + Y absorbed on the surface of (Fe, Mn)-oxyhydroxide particles was not in exchange equilibrium with REE + Y dissolved in ambient seawater (Bau and Dulski, 1996; Bau et al., 2014). In addition, the sorption of Fe-P facies is also believed to result in a positive Y anomaly.

The patterns of molybdenum-uranium covariation depend on the degree of enrichment of authigenic molybdenum (Mo_{auth}) and uranium (U_{auth}), which can be linked to specific attributes and processes of the depositional system. The dominant removal process of U involve precipitation in the sediments rather than scavenging from the water column (Anderson et al., 1989). In suboxic bottom waters, U_{auth} enrichment tends to exceed that of Mo_{auth} owing to onset of U_{auth} accumulation at the Fe^{2+}-Fe^{3+} redox boundary, leading to sediment $(Mo/U)_{auth}$ ratios less than that of seawater (Algeo and Tribovillard, 2009). In the Mo-U covariation diagram (Fig. 9), most samples especially Mn-bearing limestones and wall rocks show relative enrichment of Mo and plot well above the seawater $(Mo/U)_{auth}$ ratio, while a small number of Mn-bearing limestones and most Mn ore samples are under the seawater $(Mo/U)_{auth}$ ratio. Previous studies suggest that the Mo concentration in ancient fine-grained sedimentary rocks can assess the depositional conditions. In view of bulk Mo concentration in all samples (from 0.84 to 24.60 ppm, average 5.72 ppm) are above the crustal average (2 ppm) and below 25 ppm, which can be explained by reducing
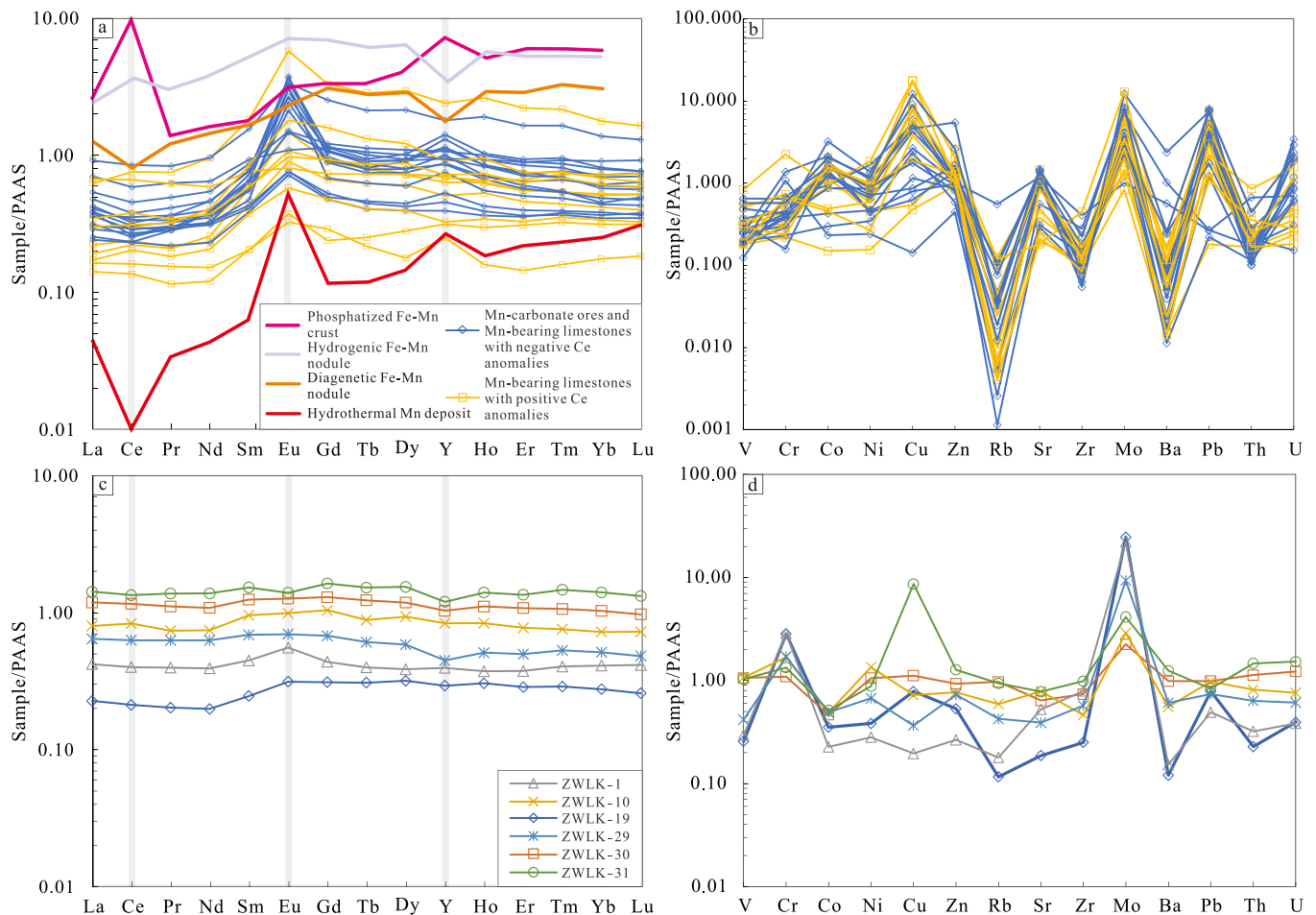
Fig. 7. PAAS-normalized REE + Y distributions of the Zhuwuluke Mn-carbonate ores, Mn-bearing limestones (a) and associated wall rocks (c). PAAS-normalized spider diagrams of trace elements of the Zhuwuluke Mn-carbonate ores, Mn-bearing limestones (b) and associated wall rocks (d). PAAS data is from (MeLennan, 1989). The heavy lines are REE + Y distributions of typical (Fe)-Mn deposits (Bau et al., 2014).

conditions where sulfide was present but restricted to the pore waters (Scott and Lyons, 2012). The strong enrichment of Mo_{auth} relative to U_{auth} in some samples including one manganese carbonate ore sample is probably due to the operation of a "particulate shuttle" linked to Mn-Fe redox cycling within the suboxic to weakly sulfidic deepwater (Algeo and Tribovillard, 2009). Burial in organic-rich sediments is a major oceanic sink for uranium, and sediments in anoxic marine basins as well as organic-rich shelf and hemipelagic sediments are enriched in uranium (Anderson, 1987). Thus, relatively high U concentration in Mn-carbonate ores may indicate they were deposited above the Fe^{2+}-Fe^{3+} redox boundary.

6.2. The origin of Mn

In assessing REE patterns for Mn deposits, one issue is mixing detrital material of different REE characteristics with the Mn ore samples. Most analyses have only minor contributions from detrital components based on low Al and Ti abundances (Fig. 6b, Table 4, Maynard, 2010). Compared with PAAS (Fig. 7), all Mn ore and Mn-bearing limestone samples show positive Eu anomalies. It is believed that hydrothermal Mn deposits commonly yield negative Ce anomalies and positive Y anomalies (Fig. 7a, Bau et al., 2014). Two factors may lead to positive Eu anomalies of Mn-bearing carbonates. One is the interference of Ba in ICP-MS detection (Nyame, 2008), and the other is hydrothermal activity (Sverjensky, 1984). The first one can be excluded by our detection measurements (Qi et al., 2000). Additionally, based on the positive correlations between Mn and δEu (Fig. 6c), we suggest that Mn^{2+} was

provided by hydrothermal sources (Michard et al., 1983) and was released through the contemporaneous faults. The developed regional faults around the mining area are ideal channels for Mn-rich hydrothermal fluids (Fig. 1b).

6.3. Mineralization process of Mn-carbonate

Crystallite Mn^{2+} carbonate dominated the Zhuwuluke manganese carbonate deposit, similar to most sedimentary manganese deposits. It is generally assumed that it is difficult for Mn^{2+} and CO_3^{2-} to precipitate directly to form Mn-carbonate deposits in ancient seawater (Dong et al., 2020; Zhang et al., 2020b), but there are few examples supporting the direct precipitation of Mn CO_3 (Van Cappellen et al., 1998; Herndon et al., 2018; Gao et al., 2021). In this study, some Mn-rich rim dolomite grains were observed under the FIB/SEM dual beam system (Fig. 4f). It was be suggested that the carbonate grain precipitated in the oxic zone acts as a nucleation site for Mn^{2+} to precipitate the observed carbonate phases with Mn-rich rim as it settles through the chemocline (Mucci, 1988), because the chemocline and monimolimnion were undersaturated with respect to calcite but oversaturated with respect to rhodochrosite and kutnohorite, reinforcing the likelihood for these carbonate phases with Mn-rich rims to form in the water column. Additionally, the formation of Mn-rich rims may preserve carbonate grains from dissolution as they settle through the euxinic botom waters where saturation indices for carbonate are below zero (Herndon et al., 2018).

Under anoxic, reducing and mild base-acidic conditions, Mn occurs in Mn^{2+} (Maynard, 2014). The oxidation of organic matter and the

Table 5

TOC and isotopic compositions for organic carbon, inorganic carbon, and oxygen in samples from the Zhuwuluke Mn ore deposit.

Sample	Sample Type	TOC (%)	$\delta^{13}C_{org}$ (V-PDB) (‰)	$\delta^{13}C_{carb}$ (V-PDB) (‰)	$\delta^{18}O_{SMOW}$ (‰)
ZWLK-1	Sandstone	0.07	−25.38	–	–
ZWLK-2	M. l.	0.18	−25.38	−12.26	23.70
ZWLK-3	M. l.	0.14	−25.76	−13.15	21.26
ZWLK-4	M. l.	0.15	−26.77	−10.14	19.75
ZWLK-5	Mn ore	0.28	−26.18	−8.81	22.05
ZWLK-6	M. l.	0.31	−24.04	−16.53	26.13
ZWLK-7	M. l.	0.14	−25.06	−9.72	17.93
ZWLK-8	Mn ore	0.21	−22.53	−9.42	23.65
ZWLK-9	M. l.	0.16	−24.51	−9.23	21.54
ZWLK-10	Siltstone	0.64	−23.75	–	–
ZWLK-11	M. l.	0.12	−25.01	−9.03	18.86
ZWLK-12	M. l.	0.11	−25.62	−14.85	25.01
ZWLK-13	M. l.	0.25	−24.96	−11.35	22.13
ZWLK-14	M. l.	0.17	−24.97	−11.53	24.48
ZWLK-15	Mn ore	0.21	−24.74	−9.46	20.93
ZWLK-16	M. l.	0.36	−25.61	−12.69	22.75
ZWLK-17	M. l.	0.21	−23.87	−16.28	24.02
ZWLK-18	Mn ore	0.13	−25.08	−7.91	20.33
ZWLK-19	Sandstone	0.03	−26.42	–	–
ZWLK-20	M. l.	0.17	−26.48	−12.42	21.47
ZWLK-21	M. l.	0.42	−25.49	–	–
ZWLK-22	Mn ore	0.32	−26.09	−12.58	27.95
ZWLK-23	M. l.	0.16	−26.09	−9.82	23.06
ZWLK-24	M. l.	0.44	−26.22	−8.80	22.77
ZWLK-25	M. l.	0.01	−25.61	−12.28	18.58
ZWLK-26	M. l.	0.01	−24.86	−9.55	19.12
ZWLK-27	M. l.	0.22	−26.37	−14.90	22.52
ZWLK-28	M. l.	0.78	−20.08	−15.57	29.87
ZWLK-29	Sandstone	0.25	−23.79	–	–
ZWLK-30	Shale	0.43	−26.70	–	–
ZWLK-31	Sandstone	0.67	−24.62	–	–

Notes: $\delta^{18}O_{SMOW}$ (‰) = $1.03092\delta^{18}O_{PDB} + 30.92$.

Table 6

Sulfur isotopic compositions of Mn-bearing carbonate and in-situ sulfur isotopic compositions of pyrite in the Mn-bearing carbonate from the Zhuwuluke Mn ore deposit.

Sample (No.)	Type	$\delta^{34}S_{V-CDT}$ (‰)	2σ
ZWLK-3	Mn-bearing limestone	−3.58	
ZWLK-3-1	Pyrite	−6.28	0.14
ZWLK-3-2	Pyrite	−5.74	0.15
ZWLK-3-3	Pyrite	−5.95	0.15
ZWLK-3-4	Pyrite	−6.46	0.15
ZWLK-9-1	Pyrite	−18.37	0.15
ZWLK-9-2	Pyrite	−18.41	0.15
ZWLK-9-3	Pyrite	−23.52	0.16
ZWLK-9-4	Pyrite	−25.29	0.16
ZWLK-11	Mn-bearing limestone	−3.10	
ZWLK-11-1	Pyrite	−3.01	0.15
ZWLK-11-2	Pyrite	−4.27	0.14
ZWLK-11-3	Pyrite	−5.82	0.15
ZWLK-11-4	Pyrite	−3.32	0.15
ZWLK-12	Mn-bearing limestone	−1.50	
ZWLK-13	Mn-bearing limestone	−18.33	
ZWLK-15	Mn ore	−11.05	
ZWLK-16	Mn-bearing limestone	−21.97	
ZWLK-23	Mn-bearing limestone	3.25	
ZWLK-26	Mn-bearing limestone	−9.77	
ZWLK-28	Mn-bearing limestone	1.56	

corresponding reduction of (Mn, Fe) (oxyhydr)oxides could have increased the Mn^{2+} concentrations in porewaters (Calvert and Pedersen, 1996). When coexisting with molecular oxygen, Mn^{2+} will be oxidized to insoluble Mn^{3+} or Mn^{4+} (oxyhydr)oxides. Frequent redox reaction cycles are able to bring evident enrichment of Mn^{2+} at the oxic to anoxic/euxinic water interface (Calvert and Pedersen, 1996). Low TOC abundances support the manganese carbonates were formed through the reduction of $Mn^{3+/4+}$ oxides, coupled to the oxidation of organic matter, following burial in anoxic sediments (Table 4, Fig. 6e, (Calvert and Pedersen, 1996)). In addition, only when Mn oxide is exhausted is there any precipitation of a mixed Mn-Ca carbonate (Shimmield and Price, 1986). Hence, it is difficult to find primitive Mn-(oxyhydr)oxides in the samples.

Relatively significant amounts of Fe-bearing Mn-carbonate in the samples indicate that Fe was not separated completely from Mn before, and/or during the deposition of the precursor Mn-(oxyhydr)oxides. Fe is commonly deposited earlier than Mn with gradual increase of oxygen fugacity (Roy, 2006). As a consequence, Mn- and Fe- (oxyhydr)oxides can be separated by an appropriate range of E_h and long distance transportation . Manganese carbonate at Zhuwuluke and Ortokarnsh ore deposits are variably, but strongly ^{13}C-depleted (Table 5, Fig. 6e). This indicates that the carbon is derived from CO_3^{2-} originating from ^{13}C-depleted organic matter deposited in sediments, with a degree of input and mixing with dissolved inorganic carbon from seawater (Nyame and Beukes, 2006). The negative carbon isotopeic ratios correlate well with high Mn contents (Fig. 10), which is attributed to the coupled reduction of Mn-(oxyhydr)oxides and oxidation of organic matter (Johnson et al., 2016). Accordingly, the Mn carbonates have been interpreted as products resulting from the reduction of precursor Mn-(oxyhydr)oxides precipitates in the presence of organic matter by heterotrophic microbes during early diagenesis (Beukes et al., 2016), and it is the main way for manganese carbonates formation at Zhuwuluke.

Two stages of separation from Fe of Mn might have played an importance role during the mineralization processes (Xu et al., 2021). Firstly, the reduced seawater became oxidized gradually, Fe^{2+} was oxidized and precipitated before Mn^{2+}, and residual Mn-rich and Fe-poor seawater flowed into the restricted basin. Secondly, at the early stage of diagenesis, organic matter was oxidized, and Mn-oxyhydroxide was reduced to form manganese carbonate. At the Dawu Mn ore deposit, H_2S was insufficient due to the extremely low sulfate concentration, and Fe^{2+} was released due to the lack of H_2S (Wu et al., 2016). However, at the Zhuwuluke Mn ore deposit, the low $^{34}\delta S$ values indicate a relatively sufficient supply of sulfate, which prevented the transportation of Fe^{2+}, resulting in higher Fe contents in Mn carbonates.

Compared with the Carboniferous Ortokarnash Mn deposit in the Western Kunlun Mountains (Zhang et al., 2020a), although hydrothermal activity played an important role in both Mn mineralization processes, the Zhuwuluke manganese carbonate deposit was deposited under deeper circumstances (hemipelagic), while the Ortokarnash Mn deposit was deposited under oxic conditions in carbonate platform. When Mn^{2+} and Fe^{2+} were enriched in bottom water in the Qiaerlong restricted basin, in-situ deposition resulted in rapid oxidation conditions for Mn-(oxyhydr)oxides, and this is may also lead to uncomplete separation of Fe from Mn at Zhuwuluke.

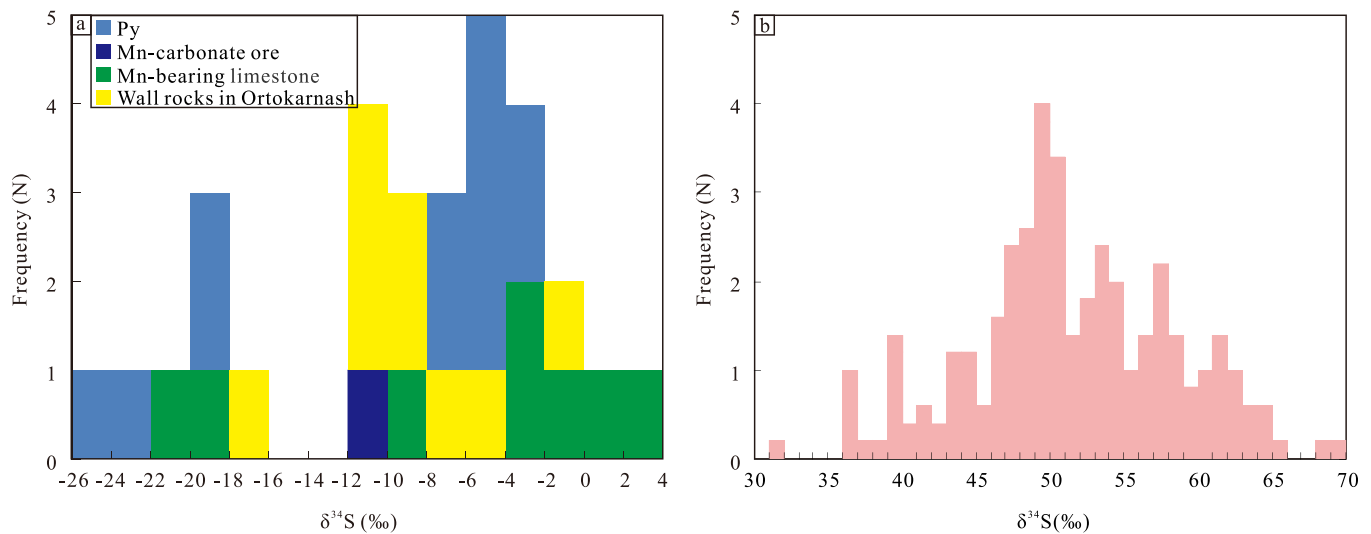According to the above, we inferred that the metallogenic process

Fig. 8. a. $\delta^{34}S_{Py}$ and bulk $\delta^{34}S$ compositions of the Zhuwuluke Mn deposit and Ortokarnash (Zhang et al., 2020); b. $\delta^{34}S_{Py}$ of Nanhuan Mn deposits hosted in the Datangpo Formation (Wu et al., 2016).

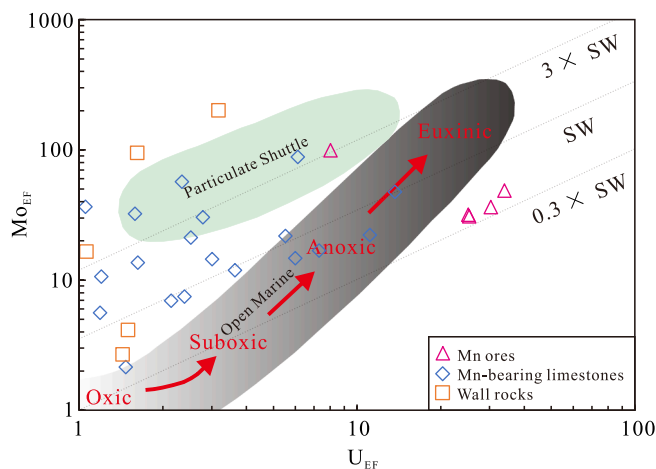**Fig. 9.** Mo_{EF} versus U_{EF} diagram for samples from the Zhuwuluke Mn deposit, modified after (Algeo and Tribovillard, 2012), restricted basin region based on Wu et al., 2016. $X_{EF} = [(X/Al)_{sample}/(X/Al)_{PAAS}]$, and X and Al represent the weight concentrations of elements X and Al, respectively. Samples were normalized using the PAAS compositions of (MeLennan, 1989). Dotted lines show Mo/U molar ratios equal to the seawater value (SW) and to fractions thereof ($0.3 \times SW$, $0.1 \times SW$) (based on Algeo and Tribovillard, 2009). Data are from Table 4.

Fig. 10. Scatter plot of $\delta^{13}C_{carb}$ values versus Mn content for the Zhuwuluke and the Ortokarnash manganese carbonate ore deposits (data of the Ortokarnash are from Zhang et al., 2020).

deposition (Johnson et al., 2016).

and mechanism at Zhuwuluke are as follows (Fig. 11): on the margin of the Qiaerlong Basin during the Early Paleozoic, hydrothermal-derived Mn^{2+} were enriched under reducing conditions in a restricted basin. Subsequently, the periodically and transiently oxic-anoxic interface declined, and Mn^{2+} and Fe^{2+} were enriched above the Fe^{2+}-Fe^{3+} redox boundary in suboxic bottomwaters as (Mn, Fe) (oxyhydr)oxides. They were buried under an underlying anoxic zone with organic matter. Relatively sufficient sulfate and rapid oxidation conditions resulted in incompleted separation of Fe from Mn. At the same time, some carbonate formed in oxic water and acted as a nucleation site for Mn^{2+} to precipitate the Mn-rich rims carbonate grains as it settled through the chemocline. During the diagenetic process, organic matter reacted with (Mn, Fe) (oxyhydr)oxides and released Mn^{2+} and Fe^{2+} (Aller and Rude, 1988), resulting in alkaline conditions (Aller, 1990). Thus, inorganic and organic bicarbonate were enriched in sedimentary porewaters, and the reduction in Mn^{4+} oxidation directly facilitated Mn carbon

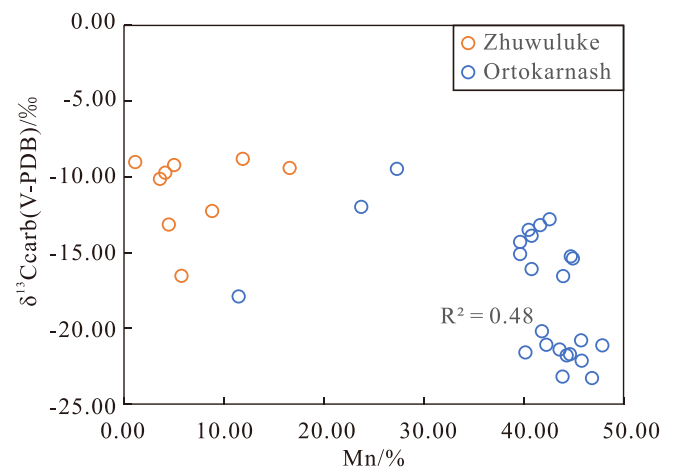## 7. Conclusion

The rocks of the Lower Carboniferous Talong Group represent sequences of hemipelagic on the margin of the Qiaerlong back-arc basin. Initially, hydrothermal Mn^{2+} was enriched under anoxic conditions and was oxidized periodically by the decline of the oxic-anoxic interface. Further reduction by organic matter transferred Mn-(oxyhydr)oxides into manganese carbonates, including rhodochrosite and kutnahorite. Due to the rapid oxidation conditions and relatively sufficient sulfate supply, the separation of Fe from Mn was incomplete. Besides, trace elements in the Mn-bearing limestones and wall rocks suggest that they were formed under reducing conditions. The variation in redox conditions and stable sedimentary environment during the Early Carboniferous collectively facilitate the formation of manganese carbonate ore deposit in the Qiaerlong Basin, Western Kunlun Mountains.

Declaration of Competing Interest

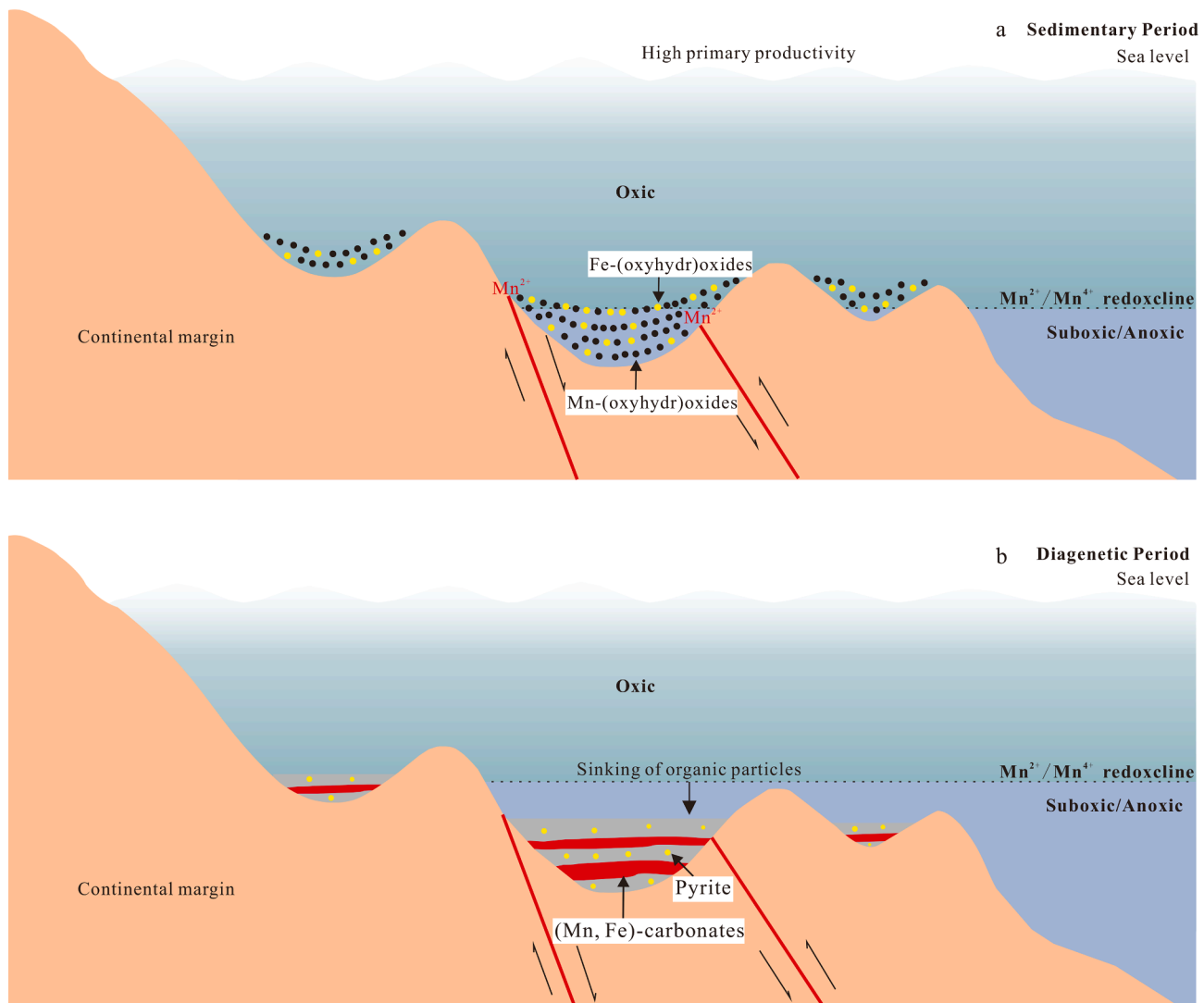The authors declare that they have no known competing financial

Fig. 11. Metallogenesis model for the Zhuwuluke Mn-carbonate ore deposit in Xinjiang Province, China (modified after Roy, 2006).

interests or personal relationships that could have appeared to influence the work reported in this paper.

References

Algeo, T.J., Tribovillard, N., 2009. Environmental analysis of paleoceanographic systems based on molybdenum–uranium covariation. Chem Geol. 268 (3-4), 211-225. https://doi.org/10.1016/j.chemgeo.2009.09.001.

Aller, R.C., 1990. The deep sea bed: its physics, chemistry and biology - Bioturbation and manganese cycling in hemipelagic sediments. Phil Trans R Soc Lond. 331 (1616), 51–68. https://doi.org/10.2307/53653.

Aller, R.C., Rude, P.D., 1988. Complete oxidation of solid phase sulfides by manganese and bacteria in anoxic marine sediments. Geochim. Cosmochim. Acta 52 (3), 751–765. https://doi.org/10.1016/0016-7037(88)90335-3.

Anderson, R.F., 1987. Redox behavior of uranium in an anoxic marine basin. Uranium 3, 145–164.

Anderson, R.F., Fleisher, M.Q., LeHuray, A.P., 1989. Concentration, oxidation state, and particulate flux of uranium in the Black Sea. Geochim. Cosmochim. Acta 53 (9), 2215–2224.

Bao, Z.A., Chen, L., Zong, C., Yuan, H., Chen, K., Dai, M., 2017. Development of pressed sulfide powder tablets for in situ sulfur and lead isotope measurement using LA-MC-ICP–MS. Int. J. Mass Spectrom. 421, 255–256. https://doi.org/10.1016/j.ijms.2017.07.015.

Bau, M., Dulski, P., 1996. Distribution of yttrium and rare-earth elements in the Penge and Kuruman iron-formations, Transvaal Supergroup, South Africa. Precambr. Res. 79 (1–2) https://doi.org/10.1016/0301-9268(95)00087-9.

Bau, M., Koschinsky, A., 2009. Oxidative scavenging of cerium on hydrous Fe oxide: Evidence from the distribution of rare earth elements and yttrium between Fe oxides and Mn oxides in hydrogenetic ferromanganese crusts. Geochem. J. 43 (1), 37–47. https://doi.org/10.2343/geochemj.1.0005.

Bau, M., Schmidt, K., Koschinsky, A., Hein, J., Kuhn, T., Usui, A., 2014. Discriminating between different genetic types of marine ferro-manganese crusts and nodules based on rare earth elements and yttrium. Chem. Geol. 381, 1–9. https://doi.org/10.1016/j.chemgeo.2014.05.004.

Beukes, N.J., Swindell, E.P.W., Wabo, H., 2016. Manganese Deposits of Africa. Episodes 39 (2), 285–317. https://doi.org/10.18814/epiiugs/2016/v39i2/95779.

Cai, T.C., 1992. Middle Devonian and Carboniferous Tetracorals from Kunlun Mountain and Karakorum Mountain, Xinjiang. (01), 51-56 (in Chinese with English abstract). https://doi.org/CNKI:SUN:XJDI.0.1992-01-005.

Calvert, S.E., Pedersen, T.F., 1996. Sedimentary geochemistry of manganese; implications for the environment of formation of manganiferous black shales. Econ Geol. 91 (1), 36–47. https://doi.org/10.2113/gsecongeo.91.1.36.

Chen, L., Yuan, H., Chen, K., Bao, Z., Zhu, L., Liang, P., 2019. In situ sulfur isotope analysis by laser ablation MC-ICPMS and a case study of the Erlihe Zn-Pb ore deposit, Qinling orogenic belt, Central China. JAESc 176, 325–336. https://doi.org/10.1016/j.jseaes.2019.02.017.

Chen, F.G., Paufahl, P.K., Wang, Q.F., Matheson, E.J., Shabaga, B.M., Zhang, Q.Z., Zeng, Y.S., Le, X.W., Ruan, D., Zhao, Y.T., 2022. A New model for the genesis of Carboniferous Mn ores, Longtou deposit, South China. Block. Econ. Geol. 117, 107–125. https://doi.org/10.5382/econgeo.4855.

Calvert, S.E., Price, N.B., 1977. Shallow Water, Continental Margin and Lacustrine Nodules: Distribution and Geochemistry. Elsevier Oceanography Series. Elsevier, pp. 45–86.

Cui, J.T., Bian, X.W., Wang, G.B., 2006. Geological composition and evolution of the West Kunlun. Shanxi Geol. 24 (1), 1-11 (in Chinese with English abstract). https://doi.org/10.3969/j.issn.1001-6996.2006.01.001.

Dewey, J.F., Shackleton, R.M., Chang, C.F., Sun, Y.Y., 1988. The Tectonic Evolution of the Tibetan Plateau. Phil Trans R Soc Lond A. 327 (1594), 379–413. https://doi.org/10.1098/rsta.1988.0135.

Dong, Z.G., Zhang, L.C., Wang, C.L., Zhang, B.L., Peng, Z.D., Zhu, M.T., Feng, J., Xie, Y.Q., 2020. Progress and problems in understanding sedimentary manganese carbonate metallogenesis. Miner. Depos. 39 (2), 237–255 (in Chinese with English abstract).

Frakes, L.A., Bolton, B.R., 1984. Origin of manganese giants: Sea-level change and anoxic-oxic history. Geology 12 (2), 83–86. https://doi.org/10.1130/0091-7613(1984)12<83:Oomgsc>2.0.Co;2.

Gao, T.B., Yang, Z., Yao, G., Zhang, Z.X., Zhu, H.Q., Wei, W., et al., 2018a. Redefinition of high pressure metamorphic rocks from West Kunlun orogen and its tectonic significance. Northwest. Geol. 51 (1), 1–12. https://doi.org/10.3969/j.issn.1009-6248.2018.01.001.

Gao, Y.B., Teng, J.X., Li, W.Y., Chen, D.H., Sui, Q.L., Jing, D.L., et al., 2018b. Geology, geochemistry and ore genesis of the Aoertuokanashi manganese deposit, West Kunlun, Xinjiang, Northwest China. Acta Petrol. Sin. 34, 2341–2358 in Chinese with English abstract.

Gao, Z., Zhu, X. Wang, D. Pan, C. Yan, B. Li, J., 2021. Insights into hydrothermal controls and processes leading to the formation of the Late Ediacaran Gaoyan stratiform manganese-carbonate deposit, Southwest China, Ore Geol. Rev. https://doi.org/10.1016/j.oregeorev.2021.104524.

Garrels, R.M., Lerman, A., 1984. Coupling of the sedimentary sulfur and carbon cycles–an improved model. Amer. J. Sci. 284 (9), 986–1007. https://doi.org/10.2475/ajs.284.9.989.

Han, F.L., 2006. Tectonic evolution and mineralization of the West Kunlun accretion-type orogen: China University of Geosciences (in Chinese with English abstract).

Haas, J., 2012. Influence of global, regional, and local factors on the genesis of the Jurassic manganese ore formation in the Transdanubian Range, Hungary. Ore Geol. Rev. 47, 77–86. https://doi.org/10.1016/j.oregeorev.2011.08.006.

Herndon, E.M., Havig, J.R., Singer, D.M., Mccormick, M.L., Kump, L.R., 2018. Manganese and iron geochemistry in sediments underlying the redox-stratified Fayetteville Green Lake. Geochim. Cosmochim. Acta 231, 50–63. https://doi.org/10.1016/j.gca.2018.04.013.

Hu, X.Y., 2009. Determine the major element concentrations of carbonate rocks using X-ray fluorescence spectrometry. Acta Mineral Sin. 598, 597 in Chinese.

Jiang, C.F., Wang, Z.Q., Li, J.Y., 2000. Opening-closing tectonics in the Central Orogenic Belt. Geological Publishing House, Beijing (in Chinese with English abstract).

Johnson, J.E., Webb, S.M., Ma, C., Fischer, W.W., 2016. Manganese mineralogy and diagenesis in the sedimentary rock record. Geochim. Cosmochim. Acta 173, 210–231.

Liu, T.-B., Maynard, J.B., Alten, J., 2006, Superheavy S isotopes from glacier-associated sediments of the Neoproterozoic of south China: Oceanic anoxia or sulfate limitation? in Kesler, S.E., and Ohmoto, H., eds., Evolution of Early Earth's Atmosphere, Hydrosphere, and Biosphere—Constraints from Ore Deposits: Geological Society of America Memoir 198, p. 205–222, doi: 10.1130/2006.1198(12).

Mao, H., 2019. The geological characteristics of Zhuwuluke manganese ore deposit in west margin of Kunlun mountains, Xinjiang. Contrib. to Geol. Mine. Resour. Res. 34 (1), 72–77 (in Chinese with English abstract).

Maynard, J.B., 2010. The chemistry of manganese ores through time: a signal of increasing diversity of earth-surface environments. Econ. Geol. 105, 535–552. https://doi.org/10.2113/gsecongeo.105.3.535.

Maynard, J.B., 2014. Manganiferous sediments, rocks, and ores. Treatise Geochem. (Second Edition). 327–349.

MeLennan, S.M., 1989. Rare earth elements in sedimentary rocks; influence of provenance and sedimentary processes. Rev. Mineral. Geochem. 21 (1), 169–200.

Michard, A., Albarède, F., Michard, G., Minster, J.F., Charlou, J.L., 1983. Rare-earth elements and uranium in high-temperature solutions from East Pacific Rise hydrothermal vent field (13 °N). Nature. 303 (30), 795–797. https://doi.org/10.1038/303795a0.

Millet, M.A., Baker, J.A., Payne, C.E., 2012. Ultra-precise stable Fe isotope measurements by high resolution multiple-collector inductively coupled plasma–mass spectrometry with a ^{57}Fe–^{58}Fe double spike. Chem. Geol. 304–305, 18–25. https://doi.org/10.1016/j.chemgeo.2012.01.021.

Mucci, A., 1988. Manganese uptake during calcite precipitation from seawater: Conditions leading to the formation of a pseudokutnahorite. Geochim. Cosmochim. Acta 52 (7), 1859–1868. https://doi.org/10.1016/0016-7037(88)90009-9.

Nyame, F., 2008. Petrography and geochemistry of intraclastic manganese carbonates from the ~2.2 Ga Nsuta deposit of Ghana: Significance for manganese sedimentation in the Paleoproterozoic of West Africa. J. Afr. Earth Sci. 50, 133–147. https://doi.org/10.1016/j.jafrearsci.2007.09.007.

Nyame, F.K., Beukes, N.J., 2006. The genetic significance of carbon and oxygen isotopic variations in Mn-bearing carbonates from the Palaeo-Proterozoic (~2.2GA) Nsuta deposit in the Birimian of Ghana. Carbonates and Evaporites 21 (1), 21–32. https://doi.org/10.1007/BF03175465.

Pan, Y.S., 2000. Geological evolution of the karakorum andkunlun mountains. Science Press, Beijing, pp. 1–539.

Pan, Y., Fang, A., 2010. Formation and evolution of the Tethys in the Tibetan Plateau. Chin. J. Geol. 45 (1), 92–101 (in Chinese with English abstract).

Qi, L., Hu, J., Conrad Grefoire, D., 2000. Determination of trace elements in granites by inductively coupled plasma–mass spectrometry. Talanta. 51, 507–513. https://doi.org/10.1016/S0039-9140(99)00318-5.

Roy, S., 2006a. Sedimentary manganese metallogenesis in response to the evolution of the Earth system. Ore Geol. Rev. 17 (3), 179–198. https://doi.org/10.1016/s0169-1368(00)00013-5.

Roy, S., 2006b. Late Archean initiation of manganese metallogenesis: its significance and environmental controls. Earth Sci. Rev. 17 (3), 179–198. https://doi.org/10.1016/j.earscirev.2006.03.004.

Scott, C., Lyons, T.W., 2012. Contrasting molybdenum cycling and isotopic properties in euxinic versus non–euxinic sediments and sedimentary rocks: refining the paleoproxies. Chem. Geol. 324, 19–27. https://doi.org/10.1016/j.chemgeo.2012.05.012.

Shimmield, G.B., Price, N.B., 1986. The behavior of molybdenum and manganese during early sediment diagenesis—offshore Baja California. Mexico. Mar. Chem. 19, 261–280.

Sholkovitz, E.R., Landing, W.M., Lewis, B.L., 1994. Ocean particle chemistry: The fractionation of rare earth elements between suspended particles and seawater. Geochim. Cosmochim. Acta 58, 1567–1579. https://doi.org/10.1016/0016-7037(94)90559-2.

Strauss, H., 1999. Geological evolution from isotope proxy signals-sulfur. Chem. Geol. 161, 89–101. https://doi.org/10.1016/S0009-2541(99)00082-0.

Sverjensky, D.A., 1984. Europium redox equilibria in aqueous solution. Earth. Planet. Sci. Lett. 67 (1) https://doi.org/10.1016/0012-821x(84)90039-6.

Van Cappellen, P., Viollier, E., Roychoudhury, A., Clark, L., Ingall, E., Lowe, K., Dichristina, T., 1998. Biogeochemical Cycles of Manganese and Iron at the OxicAnoxic Transition of a Stratified Marine Basin (Orca Basin, Gulf of Mexico). Environ Sci Technol. 32 (19), 2931–2939. https://doi.org/10.1021/es980307 m.

Wilkin, R.T., Barnes, H.L., Brantley, S.L., 1996. The size distribution of framboidal pyrite in modern sediments: An indicator of redox conditions. Geochim. Cosmochim. Acta 60 (20), 3897–3912. https://doi.org/10.1016/0016-7037(96)00209-8.

Wilkin, R.T., Arthur, M.A., Dean, W.E., 1997. History of water-column anoxia in the Black Sea indicated by pyrite framboid size distributions. Earth Planet. Sci. Lett. 148, 517–525. https://doi.org/10.1016/S0012-821X(97)00053-8.

Wu, C., Zhang, Z., Xiao, J., Fu, Y., Shao, S., Zheng, C., Yao, J., Xiao, C., 2016. Nanhuan manganese deposits within restricted basins of the southeastern Yangtze Platform, China: Constraints from geological and geochemical evidence. Ore Geol. Rev. 75, 76–99.

Lu, S.W. Du, F.J. Ren, J.D. The Regional Geological Survey of the People's Republic of China about Yingjisha and Atikairdingsayi (1:250000) 2013 Wuhan.

Xie, R.S., Wang, H.C., Wu, C.W., Yang, W.C., 2018. Analysis of oil-forming conditions of carboniferous Taalong Group source rocks in West Kunlun, Xinjiang. Xinjiang nonferrous metals, 2, 5-6 (in Chinese). https://doi.org/10.16206/j.cnki.65-1136/tg.2018.02.003.

Xu, J.H., Zhang, Z.W., Wu, C., Zhu, W.G., Luo, T.Y., Hu, P.C., Li, X.Y., Jin, Z.R., 2019. The genesis of the early Paleozoic granitoid: Evidence from the petrogeochemistry, chronology, and Sr-Nd-Hf isotope. The 9th National Symposium on metallogenic Theory and Prospecting Methods. Nanjing. pp. 284-285.

Xu, J.H., Zhang, Z.W., Wu, C., Li, X.Y., Jin, Z.R., Hu, P.C., Luo, T.Y., Zhu, W.G., 2021a. Petrogenesis and tectonic implications of Early Paleozoic granitoids in the Qiaerlong district of the West Kunlun orogenic belt: constraints from petrology, geochronology, and Sr-Nd-Hf isotope geochemistry. Int. Geol. Rev. 1–22 https://doi.org/10.1080/00206814.2021.1882888.

Xu Q, Z, Li T, S, Zhang X, J, Yang S, J, He Z, B, Li B, H, Lin S, C, Cai H, Z, 2011. Paleo-Asian and Tethyan tectonic systems with docking the Tarim block. Acta Petrologica Sinica 27 (1), 1–22. CNKI:SUN:YSXB.0.2011-01-002.

Xu, Z., Wu, C., Zhang, Z., Xu, J., Li, X., Jin, Z., 2021b. Separation of Fe from Mn in the Cryogenian Sedimentary Mn Deposit, South China: Insights from Ore Mineral Chemistry and S Isotopes from the Dawu Deposit. Minerals 11, 446. https://doi.org/10.3390/min11050446.

Yan, H., Pi, D.-H., Jiang, S.-Y., Mao, J.W., Xu, L.G., Yang, X.Q., Hao, W.D., Mand, K., Li, L., Konhauser, O.K., Robbins, L.J., 2022. Mineral paragenesis in Paleozoic manganese ore deposits: Depositional versus post-depositional formation processes. Geochim. Cosmochim. Acta 325, 65–86. https://doi.org/10.1016/j.gca.2022.03.030.

Ye, L., Fan, D., Yang, P., 1988. Characteristics of manganese ore deposits in China. Ore Geol. Rev. 4 (s 1–2), 99–113. https://doi.org/10.1016/0169-1368(88)90006-6.

Zhang, B.-L., Wang, C.-L., Robbins, L.J., Zhang, L.-C., Konhauser, K.O., Dong, Z.-G., Li, W.J., Peng, Z.D., Zheng, M.T., 2020a. Petrography and Geochemistry of the Carboniferous Ortokarnash Manganese Deposit in the Western Kunlun Mountains, Xinjiang Province, China: Implications for the Depositional Environment and the Origin of Mineralization. Econ. Geol. 115 (7), 1559–1588. https://doi.org/10.5382/econgeo.4729.

Zhang, L.C., Zhang, B.L., Dong, Z.G., Xie, Y.Q., Li, w.j., Peng, Z.D., Zhu, M.T., Wang, C.L., 2020b. Tectonic setting and metallogenetic conditions of Carboniferous malkansu giant manganese belt in West Kunlun orogen. J. Jilin Univ. (Earth Sci. Edit.). 50 (5), 1340-1357 (in Chinese with English abstract). https://doi.org/10.18814/epiiugs/2016/v39i2/95779.

Zhang, Z., Yang, X., Zhang, L., Wu, C., Luo, T., Zhu, W., Xu, J., Hu, P., Li, X., Jin, Z., 2021. Sedimentation and mineralization of the Late Paleozoic extensional basin in the western Kunlun Mountains, China. Solid Earth Sci. 6 (2), 142–177.